NASA Contractor Report 156886 (II)

(NASA-CR-156886-Vol-2) NOSS ALGORITHM SPECIFICATIONS FOR OCEAN CURRENT MAPPING, VOLUME 2 (Analytic Sciences Corp.) 108 p
HC A06/MF A01 CSCL 08C

N82-30824

Unclas
G3/48 28728

NOSS Algorithm Specifications for Ocean Current Mapping

Volume II

James V. White

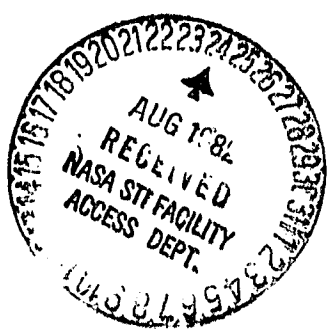

July 1982

National Aeronautics and Space Administration

Goddard Space Flight Center
Wallops Flight Center
Wallops Island, Virginia 23337

NASA Contractor Report 156886 (II)

NOSS Algorithm Specifications for Ocean Current Mapping

Volume II

James V. White

The Analytic Sciences Corporation
One Jacob Way
Reading, Massachusetts 01867

Prepared Under Contract No. NAS6-3163

National Aeronautics and
Space Administration

Goddard Space Flight Center
Wallops Flight Center
Wallops Island, Virginia 23337

TABLE OF CONTENTS

TABLE OF CONTENTS (Continued)

LIST OF FIGURES

LIST OF FIGURES (Continued)

LIST OF FIGURES (Continued)

LIST OF TABLES

1. INTRODUCTION

1.1 BACKGROUND AND INVESTIGATION OBJECTIVES

The satellite microwave altimeters aboard GEOS-3 and SEASAT provided nearly global data on sea surface height (SSH) with respect to the reference ellipsoid. The altimeter data were used for a variety of oceanographic investigations, e.g., Gulf-Stream dynamics (Ref. 1), estimation of mean sea surfaces (Refs. 2 and 3), and SSH mesoscale variability (Refs. 4 and 20).

The feasibility of detecting and locating dynamic ocean currents using SSH data has been demonstrated with GEOS and SEASAT altimetry (e.g., Refs. 5 and 6). Proposed future satellite altimeter missions, such as the National Oceanic Satellite System (NOSS), would provide global SSH data for both oceanographic research and the generation of operational products (e.g., maps of geostrophic boundary currents, ring currents, and geostrophic velocity estimates).

The purpose of this investigation is twofold:

- Quantify the oceanographic information content of SEASAT altimeter SSH data
- Develop and verify algorithms, suitable for use by NOSS, for automatically detecting and locating geostrophic ocean currents, eddy boundaries and rings, and for estimating geostrophic velocities from single tracks of satellite altimeter SSH data.

1.2 TECHNICAL APPROACH

The technical approach used in this investigation is based on three complementary techniques:

- Autoregressive statistical modeling of the altimeter data
- Matched-filter signal detectors for optimally discriminating between noise and ocean-current signatures in the altimeter data
- Kalman smoothing techniques for estimating oceanographic signal waveforms in the altimeter data.

The application of these techniques is outlined in the following three sections.

1.2.1 Study of the Oceanographic Information Content of SEASAT Altimeter Data

SEASAT altimeter data along nearly repeating ground tracks (repeat-track data) are used to study the oceanographic information content of the altimeter data. Geoid profiles are subtracted from each track of altimeter data. The statistical properties of the resulting residual time series are quantified by using autoregressive (AR) modeling to estimate the power spectrum of the residual data process. In addition, quantile-quantile plots are computed to characterize the probability distribution of the residuals.

To reduce the geoid modeling errors to negligible magnitudes and to provide direct observations of the temporal variability of the oceanographic signals in the residual data, the data from repeating tracks are averaged, and the deviations of each track of data from this average are computed.

The statistics of the resulting difference data are analyzed by autoregressive modeling, and Kalman-smoothing techniques are used to estimate the waveforms in the data caused by mesoscale time-varying signal components.

1.2.2 Development of an Ocean-Current Detection Algorithm

Matched-filtering techniques are used to develop an ocean-current detection algorithm that incorporates both deterministic and statistical information about the ocean currents, the altimeter data, and the estimated geoid profiles. This approach is flexible and suited for both boundary currents and eddies. The matched-filtering approach is optimal with respect to reasonable models for the noise signals and the ocean-current signatures in the altimeter data.

1.2.3 Development of a Geostrophic-Velocity Estimation Algorithm

A bank of matched filters is used to detect the boundary current signature in the altimeter data and to compute maximum-likelihood estimates of the coefficients of a parametric model signature. The sea-surface slope is estimated from the parametric signature model, and the geostrophic equation yields an estimate for the cross-track component of the geostrophic current velocity.

1.3 ORGANIZATION OF REPORT

The report is organized as follows. The study of the oceanographic information content of SEASAT altimeter data is described in Chapter 2. These results provide the foundation for the ocean-current detection algorithm, the development and

verification of which is presented in Chapter 3. Chapter 4 summarizes the development of the geostrophic-velocity estimation algorithm and its verification with SEASAT altimeter data in the western North Atlantic. The report concludes with a summary, conclusions, and suggestions for further study in Chapter 5.

2. OCEANOGRAPHIC INFORMATION CONTENT

2.1 INTRODUCTION

The approach for determining the oceanographic information content of SEASAT altimeter data starts with the selection of tracks for analysis from areas for which TASC has precise local geoid models. Geoid profiles are subtracted from each track of altimeter data to yield residual data sets, which consist of oceanographic signals as well as error signals caused by such factors as residual geoid modeling errors, orbit uncertainties, instrumentation noise, and errors in corrections for tides, barotropic pressure, and atmospheric influences.

To study the signal components caused by time-varying oceanography, the residual data are analyzed along nearly repeating tracks at 3-day intervals. Repeat-track analysis consists of first computing the point-wise ensemble mean of all the tracks in a given set. This ensemble mean is a time series that consists primarily of geoid modeling error together with the mean dynamic sea surface topography. The second step is to subtract this mean time series from each track in the set. The resulting difference data show how each track differs from the ensemble mean. These tracks of difference data give direct observations of the time-varying components of oceanography in the original altimeter data.

The time-varying oceanographic signals in the difference data are caused by both mesoscale and microscale variations in sea surface height. To determine the distribution of power with wavelength, the difference data are spectrally analyzed

by using autoregressive (AR) modeling techniques. The resulting AR models yield an estimated power spectrum for each track. The differences among these spectra quantify the changes in the distribution of power in the oceanographic signals from one track to the next. The differences among these spectra may also be caused, in part, by time-varying residual error signals associated with the data corrections for atmospheric effects and instrument errors (as provided in the Geophysical Data Records).

The power spectra provide estimates of the average power distribution in the difference data for wavelengths ranging from approximately 1500 km to 14 km. Based on this information, optimal Kalman smoothers are designed to extract the mesoscale (correlated) signal waveforms in each track of data. The optimal smoothers also compute theoretical rms values for the errors in the estimated mesoscale waveforms. These data provide direct quantitative measures of the oceanographic information content of the SEASAT altimeter data.

2.2 SELECTED SEASAT ALTIMETER DATA

Twenty-nine tracks of SEASAT altimeter data (1 sample/second) were analyzed. These tracks were selected in the Gulf of Alaska and the North-Atlantic region south of Iceland, areas for which TASC has precise local 5-min gravimetric geoid estimates. Figures 2.2-1 and 2.2-2 show maps of these regions with 500-meter bathymetry contours. The selected SEASAT tracks are labeled with their REV numbers.

Geoid profiles were computed along each track by using bilinear interpolation on precise 5-min local gravimetric geoid estimates. An example of a geoid profile is shown in Fig. 2.2-3

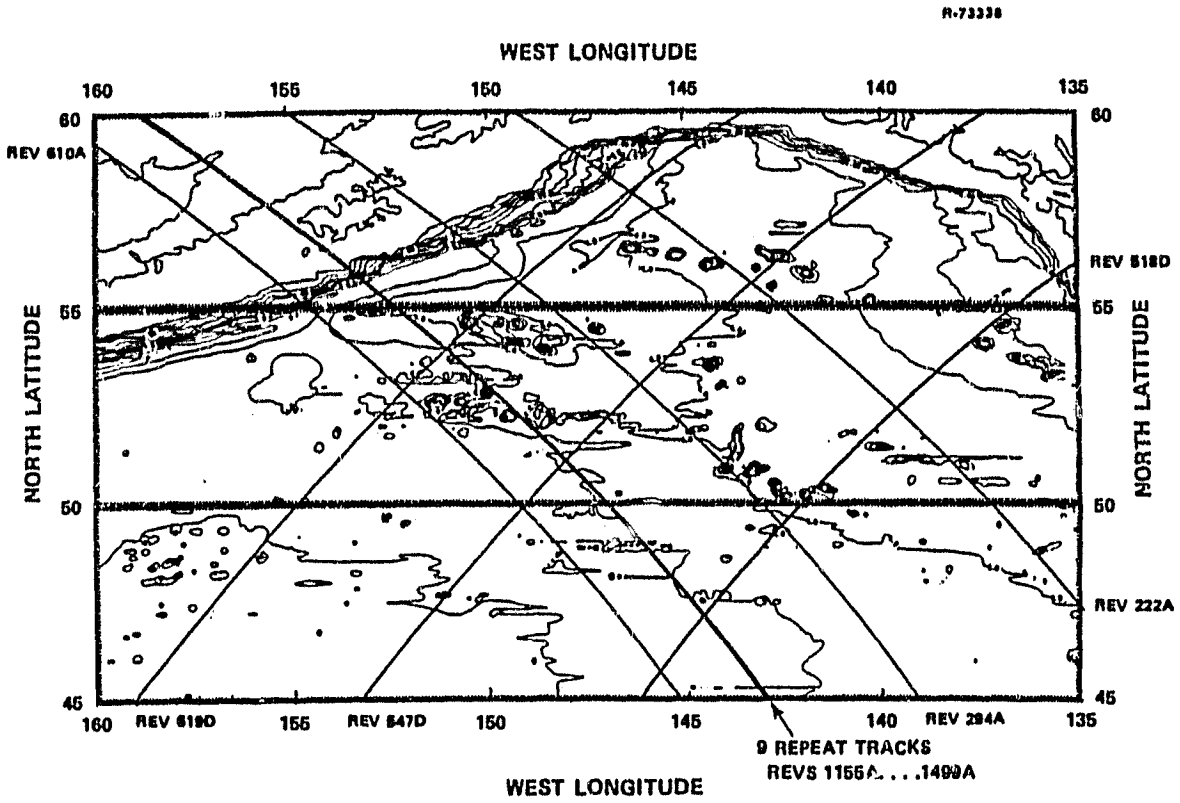

Figure 2.2-1 SEASAT Tracks and 500-Meter Bathymetry Contours for Gulf of Alaska

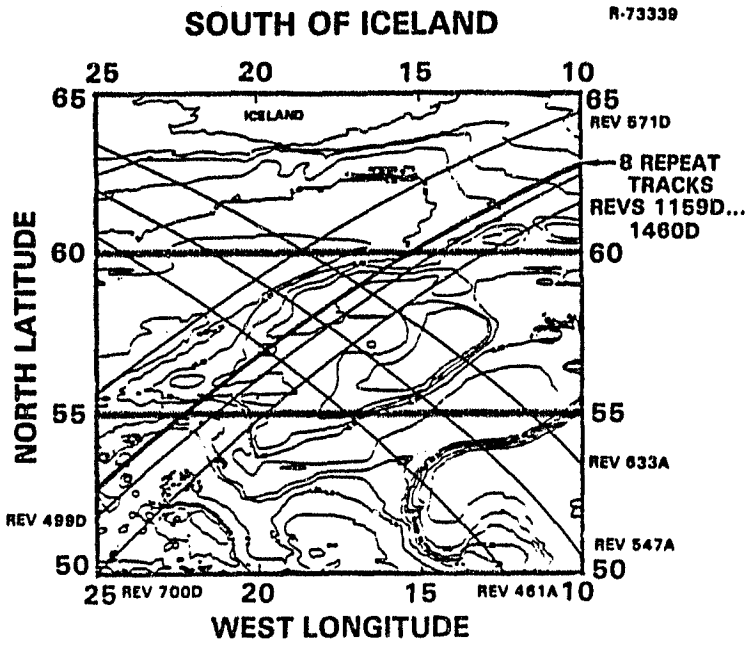

Figure 2.2-2 SEASAT Tracks and 500-Meter Bathymetry Contours for North Atlantic

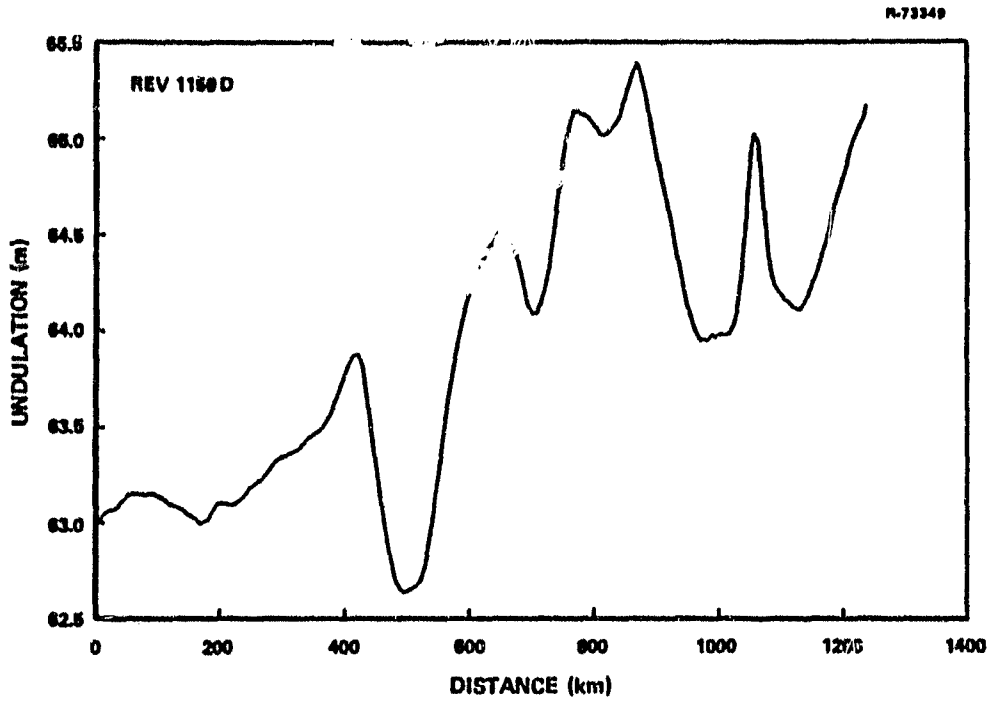

Figure 2.2-3 Geoid Profile for SEASAT Rev. 1159D in North Atlantic

for Rev. 1159D in the North Atlantic. The corresponding track of SEASAT altimeter data is shown in Fig. 2.2-4. Subtracting the geoid profile from the altimeter data produces the residual data shown in Fig. 2.2-5. The abrupt 0.4-meter feature located at 1050 km in Fig. 2.2-5 is caused by a seamount, while the offset and linear trend in this figure are attributed primarily to radial orbit uncertainty and long-wavelength geoid estimation error. The process of subtracting geoid profiles was carried out for all of the Revs. shown in Figs. 2.2-1 and 2.2-2. The resulting collection of SEASAT-minus-geoid residual data forms the basis for the analyses described in the following sections of this chapter.

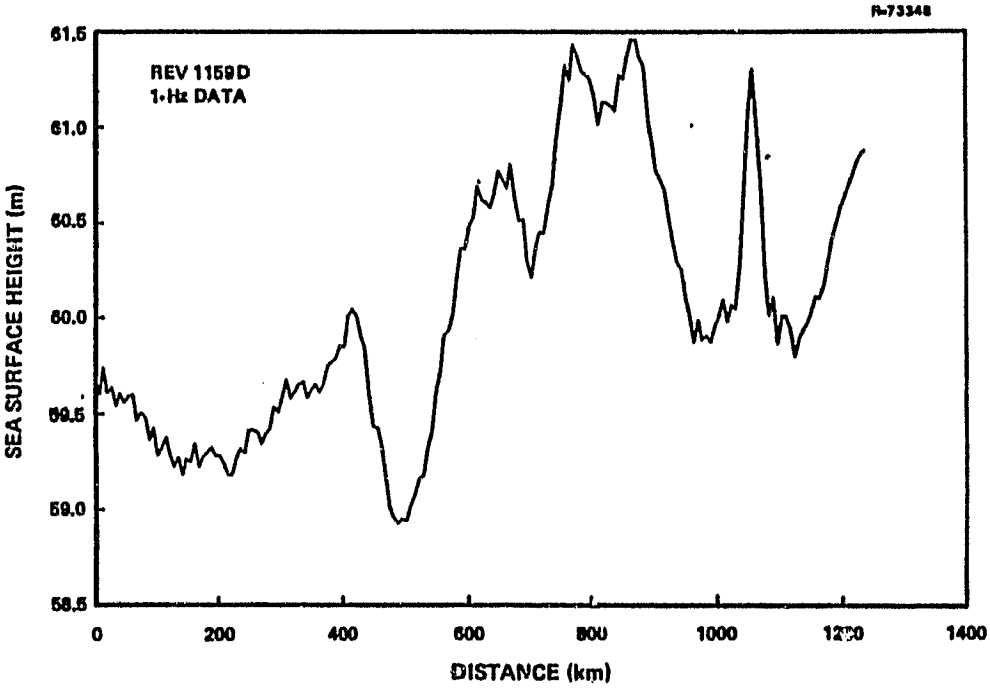

Figure 2.2-4 SEASAT Altimeter Data for Rev. 1159D in North Atlantic

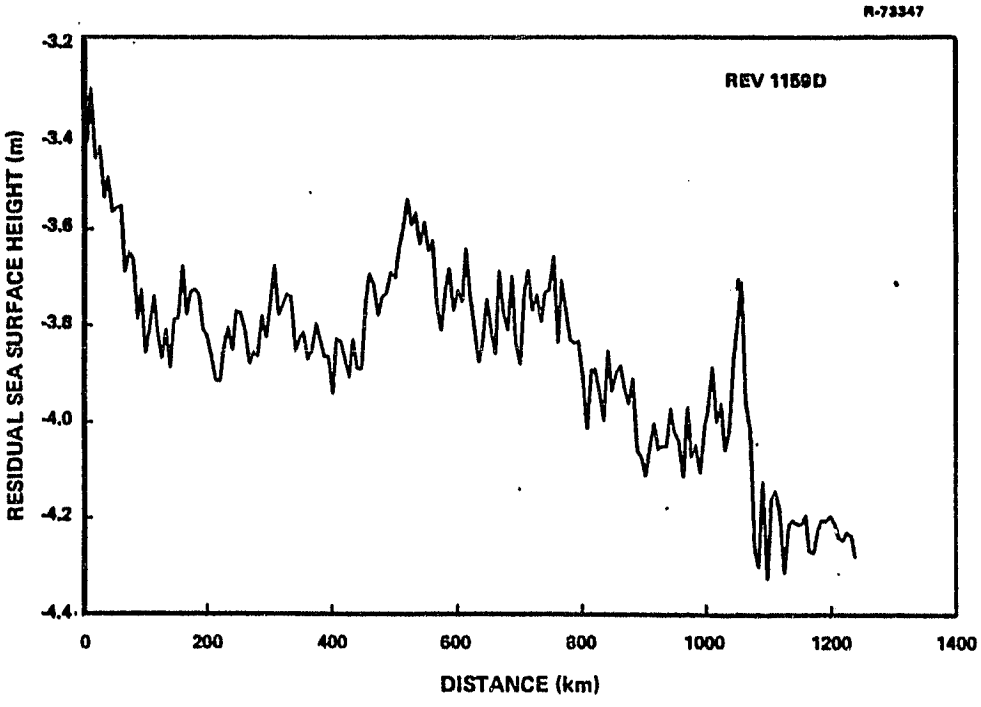

Figure 2.2-5 SEASAT-Minus-Geoid Residual Data for Rev. 1159D in North Atlantic

2.3 REPEAT-TRACK DATA

In the Gulf-of-Alaska region, nine of the satellite tracks (spanning 15 September - 7 October) were nearly repeating with an rms separation of 1.9 km. Eight more repeat tracks (spanning 16 September - 7 October) were available in the North-Atlantic region with an rms separation of 3.1 km. To analyze the time-varying oceanographic signals in these data, the long-wavelength errors caused by radial orbit uncertainties were attenuated by subtracting a least-squares linear trend from each track of data. The resulting sets of residual data are shown in Figs. 2.3-1 and 2.3-2. For clarity, the plots are vertically offset from each other by 0.5 m. There are common features shared by all tracks in each set; these features are attributed to geoid estimation error and the mean sea-surface height signature.

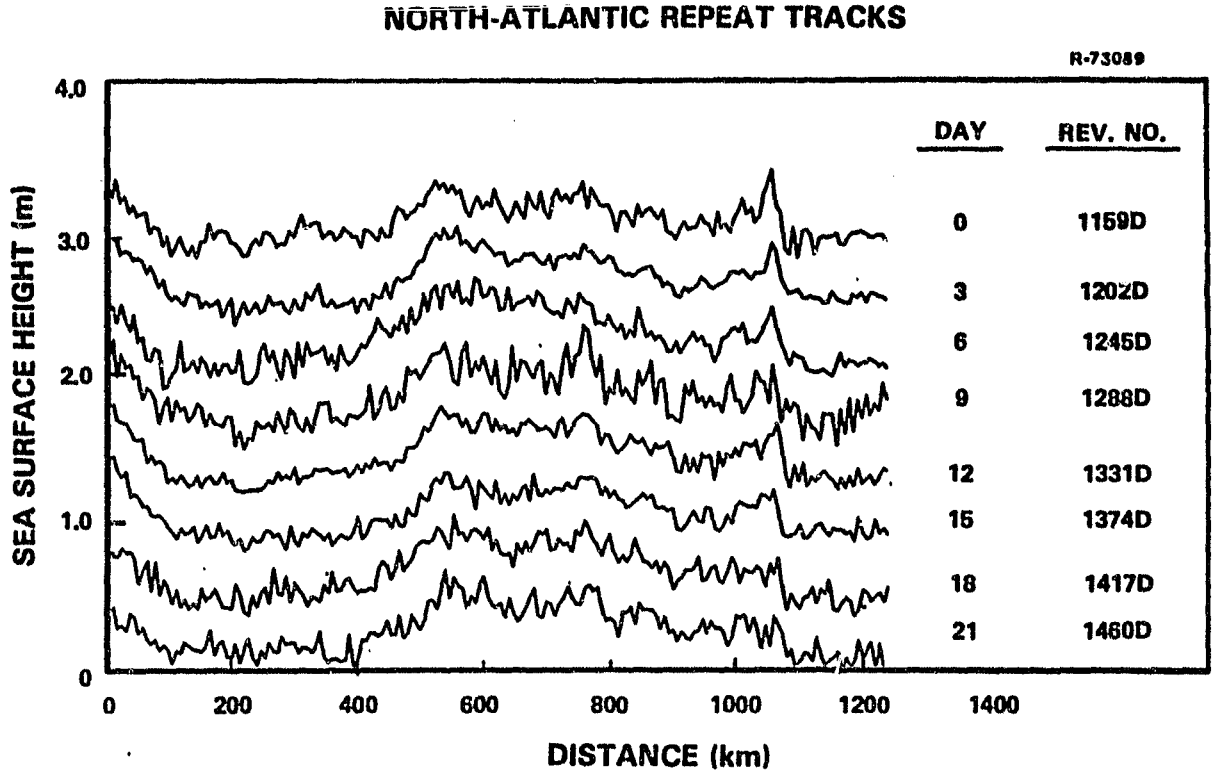

Figure 2.3-1 Ensemble of Detrended SEASAT-Minus-Geoid Residuals for Repeat Tracks in North Atlantic

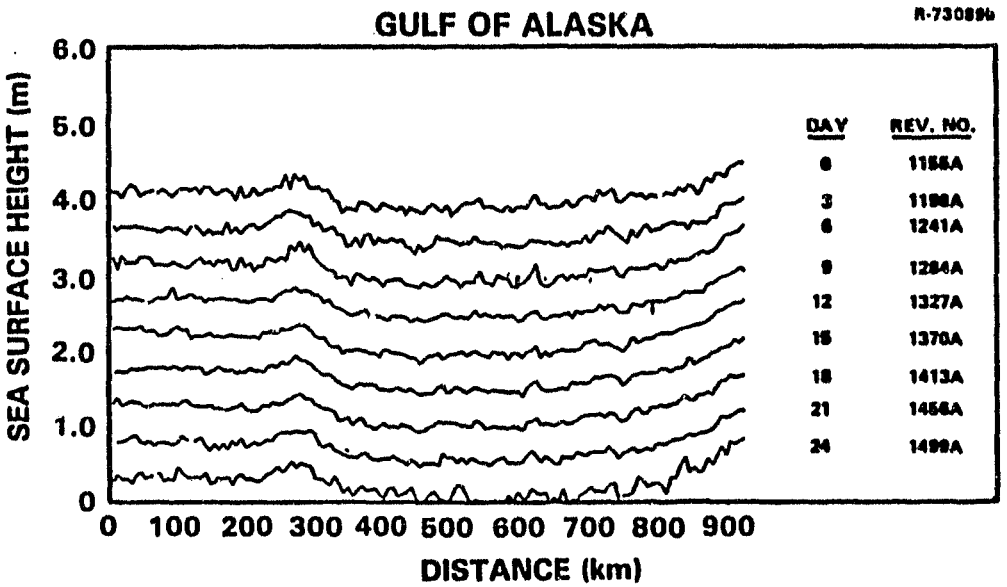

Figure 2.3-2 Ensemble of Detrended SEASAT-Minus-Geoid Residuals for Repeat Tracks in Gulf of Alaska

2.4 AUTOREGRESSIVE DATA ANALYSIS

To determine the distribution of average signal power with wavelength (frequency), selected tracks of data were statistically analyzed by using an autoregressive modeling technique. This method of spectrum estimation is better suited for the analysis of individual tracks of data than the classical method based on periodgrams.

An autoregressive (AR) model of order p for a time series D(t), t = 1,..., N, is the difference equation

$$D(t) = \sum_{k=1}^{p} C_k D(t-k) + w(t), \quad t = p+1, \ldots, N \qquad (2.4\text{-}1)$$

where

$w(t)$ = residual noise

The coefficients C_k, $k = 1,\ldots, p$, are chosen to minimize the mean-square residuals (COVAR algorithm, Ref. 9)

$$VAR = \frac{1}{N-p} \sum_{t=p+1}^{N} w^2(t) \qquad (2.4\text{-}2)$$

If the AR model is appropriate for the process generating the data, then the residuals $w(t)$, $t = p+1,\ldots, N$, are a sample of approximately white noise. It follows that the power spectral density (power spectrum) of the discrete-time process generating the data $D(t)$ can be estimated as

$$S_o(F) = \frac{\overline{VAR}}{\left|1 - \sum_{k=1}^{p} C_k \, e^{i2\pi Fk}\right|^2} \qquad (2.4\text{-}3)$$

where

F = dimensionless frequency (cycles/sample) (2.4-4)

$F = 0.5$ is the folding frequency. The variance of the random process having the power spectrum $S_o(F)$ is

$$\text{variance} = \int_{-\frac{1}{2}}^{\frac{1}{2}} S_o(F)dF \qquad (2.4\text{-}5)$$

A natural estimate for the power spectrum of the underlying continuous-time process (of which the data $D(t)$ are uniformly-spaced sample values) is

$$S(f) = S_o(f/f_s)/f_s, \quad |f| \leq \frac{f_s}{2} \qquad (2.4\text{-}6)$$

where

f_s = data sampling frequency = 1.0 Hz

f = spectrum frequency in hertz

The altimeter data D(t) are measured in meters, and it follows that S(f) has the units m^2/Hz. The wavelength λ corresponding to frequency f is

$$\lambda = v/f \qquad (2.4\text{-}7)$$

where

v = altimeter subtrack velocity = 6700 m/s (2.4-8)

For each track of data, the best choice of the AR model order p is estimated by computing the Akaike information criterian (AIC) for a family of AR models, p = 0,..., N/20 (Refs. 10-12):

$$AIC = N \log_e(VAR) + 2p \qquad (2.4\text{-}9)$$

The model for which AIC is smallest is chosen as the best AR model for the underlying process that generated the observed data D(t).

Several applications of this AR-modeling technique to the analysis of SEASAT data are described in the following sections of this chapter.

2.5 PROBABILITY DENSITY FUNCTION OF RESIDUAL ALTIMETRY

Selected tracks of SEASAT-minus-geoid residual altimeter data were analyzed to determine if their statistical behavior is nearly Gaussian. Information about the probability distribution of the residual altimeter data is needed for designing optimal algorithms for detecting and estimating ocean currents and for computing the theoretical performance of these algorithms.

To investigate the probability distribution of the altimeter data, the following approach was used:

- Each track of residual altimetry was approximately whitened by applying a suitable linear transformation to the data. This linear transformation was determined from the minimum-AIC AR data model and was unique for each track of data. Mathematically stated, the data D(t) were transformed to the nearly white sequence w(t) by using the AR equation

$$w(t) = D(t) - C_1 D(t-1) - \ldots - C_p D(t-p) \qquad (2.5\text{-}1)$$

  where the coefficients C_k, $k = 1,\ldots,p$, and the order p were determined as described in Section 2.4.

- The whitened data w(t) were then analyzed to determine how nearly their empirical distribution function matched the normal (Gaussian) distribution. The use of whitened data is necessary because the statistical tests for normality are based on the assumption that the data are statistically independent samples.

The whitened data w(t) were listed in order from smallest to largest. These ordered values were then plotted versus

their theoretical deviation from the median, expressed in standard deviations (quantiles) of the normal probability distribution. The resulting graph is called a normal QQ plot, and (as depicted in Fig. 2.5-1) it shows departures of the data values from a normal distribution. Nearly Gaussian data yield a nearly straight line, while short- or long-tailed empirical distributions produce marked deviations from the straight line.

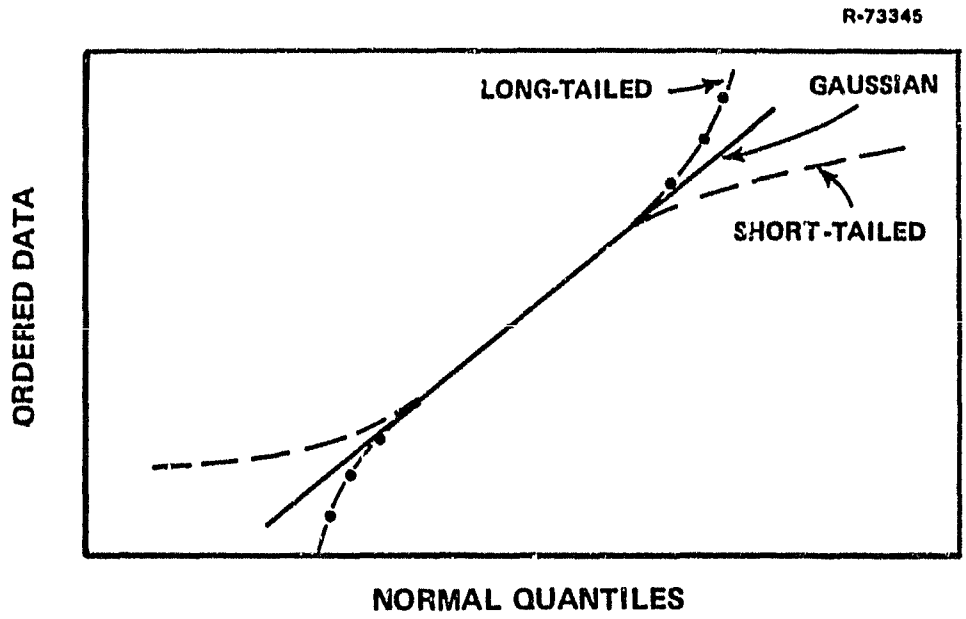

Figure 2.5-1 Example QQ Plots

A typical QQ plot for residual SEASAT altimeter data is shown in Fig. 2.5-2; the plot indicates nearly Gaussian behavior. In contrast, Fig. 2.5-3 shows the worst-case (least Gaussian) result for all the tracks analyzed. The departures from Gaussian behavior are caused by atypical events such as the occurrence of data errors, extreme weather, and seamounts.

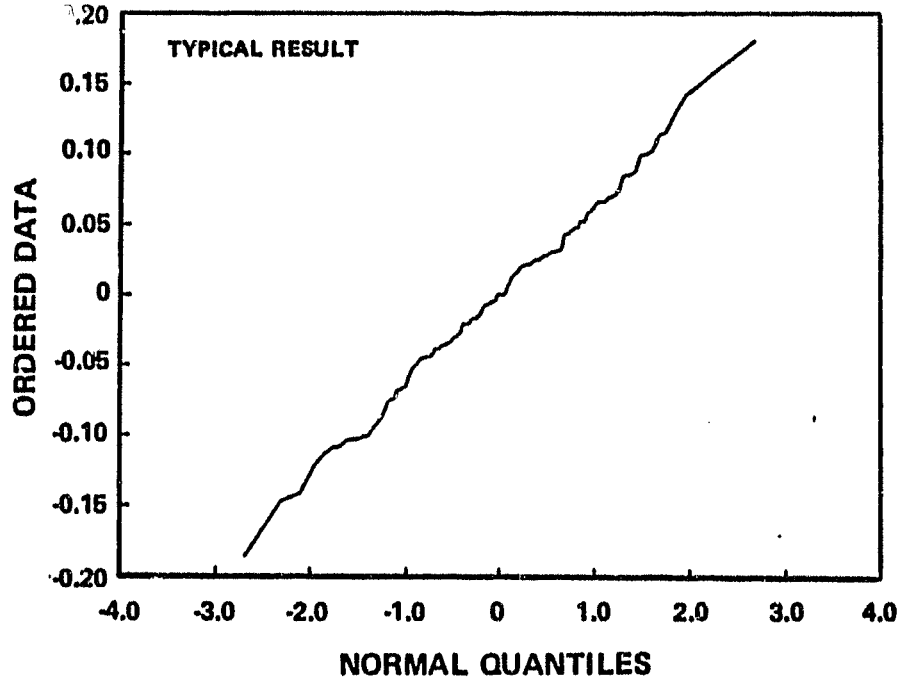

Figure 2.5-2 Typical QQ Plot of Residual SEASAT Altimeter Data

R-73344

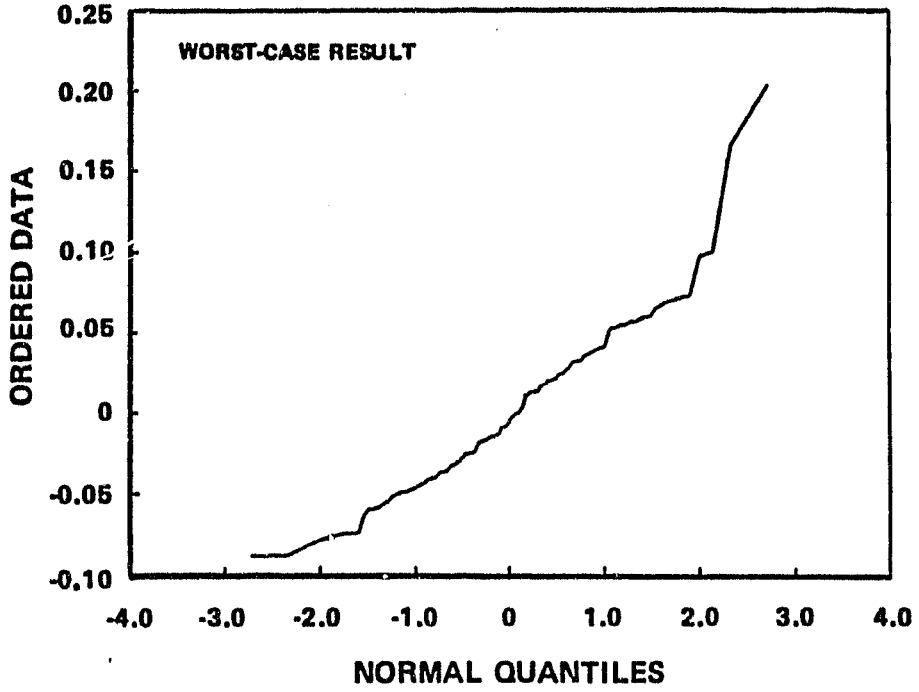

Figure 2.5-3 Atypical QQ Plot of Residual SEASAT Altimeter Data Showing Departure from Gaussian Behavior

The conclusion reached from this analysis is that both Atlantic and Pacific residual altimeter data are nearly Gaussian in their statistical behavior. No systematic departure from Gaussian behavior was detected.

2.6 ANALYSIS OF TEMPORAL VARIABILITY IN REPEAT-TRACK DATA

To study the time-varying signals in the repeat-track residuals, an ensemble-mean time series X was computed for each set of repeat-track residual data:

$$X(t) = \frac{1}{m} \sum_{j=1}^{m} x_j(t), \quad t = 1,\ldots, N \qquad (2.6\text{-}1)$$

where

$x_j(t)$ = t-th datum in j-th track of residual data

m = number of repeat tracks in set

N = number of data in each track.

The ensemble-mean series was then subtracted from each track of residual data to produce the difference-data time series D_j:

$$D_j(t) = x_j(t) - X(t), \quad j = 1,\ldots, m, \; t = 1,\ldots, N \qquad (2.6\text{-}2)$$

The $D_j(t)$ time series (difference data) are direct observations of the time-varying oceanography in the original altimeter data. Because of the differencing operations, these difference data contain a negligible signal component caused by geoid estimation error. (The residual geoid estimation error in the

difference data has an estimated rms value of less than 0.3 cm based on the known rms separations of the repeat tracks and the known rms value of the first differences (X(t-1) - X(t)) of the ensemble-mean time series.)

An example of SEASAT difference data is shown in Fig. 2.6-1 for Rev. 1159D in the North Atlantic. Because these data have a significant uncorrelated signal component, each data sample is plotted for clarity as a vertical spike. The rms value of these data is 6.4 cm. The average rms value for the ensemble of eight tracks of difference data in the North-Atlantic region is 6.3 cm, the smallest rms value is 4.4 cm, the largest is 9.2 cm. In the Gulf-of-Alaska region the average rms value for the nine repeat tracks of difference data is 4.2 cm, the smallest rms value is 3.0 cm, the largest is 6.5 cm, and the standard deviation of the rms values is 1.2 cm.

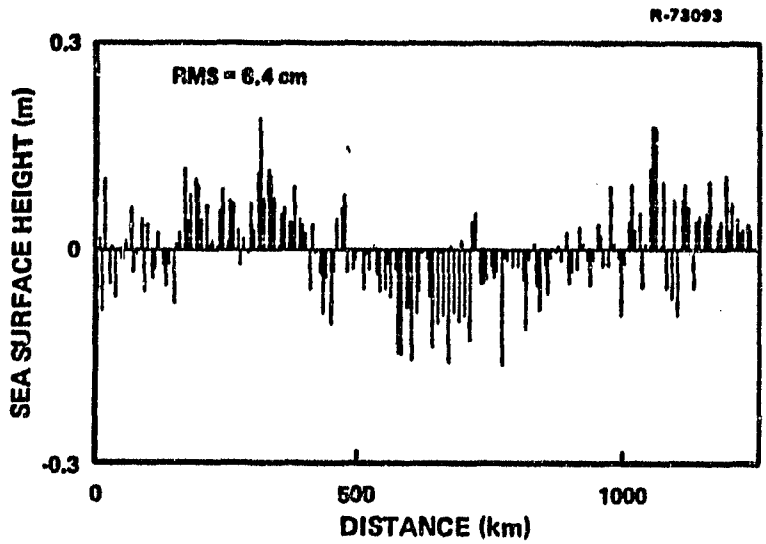

Figure 2.6-1 Difference Data for Rev. 1159D in North Atlantic

An AR spectrum estimate from the difference data along Rev. 1159D in the North-Atlantic region is shown in Fig. 2.6-2. This spectrum is representative of those computed for the other repeat tracks. The spectrum attains its largest values on the plateau at low frequencies (wavelengths greater than 1000 km). There is a downward transition to another plateau at high frequencies (wavelengths shorter than 100 km). This high-frequency plateau is sometimes obscured by ripples in the spectrum estimate, as seen, e.g., in Fig. 2.6-2. These ripples may be caused in part by the inherent sampling variability of the spectrum estimator. The ripples may also be caused in part by high-frequency structure in the altimeter data. In either case, the overall structure of each AR spectrum estimate is represented by a white-noise floor at high frequencies plus a 1st-order Markov spectrum that models the transition to the raised plateau at low frequencies.

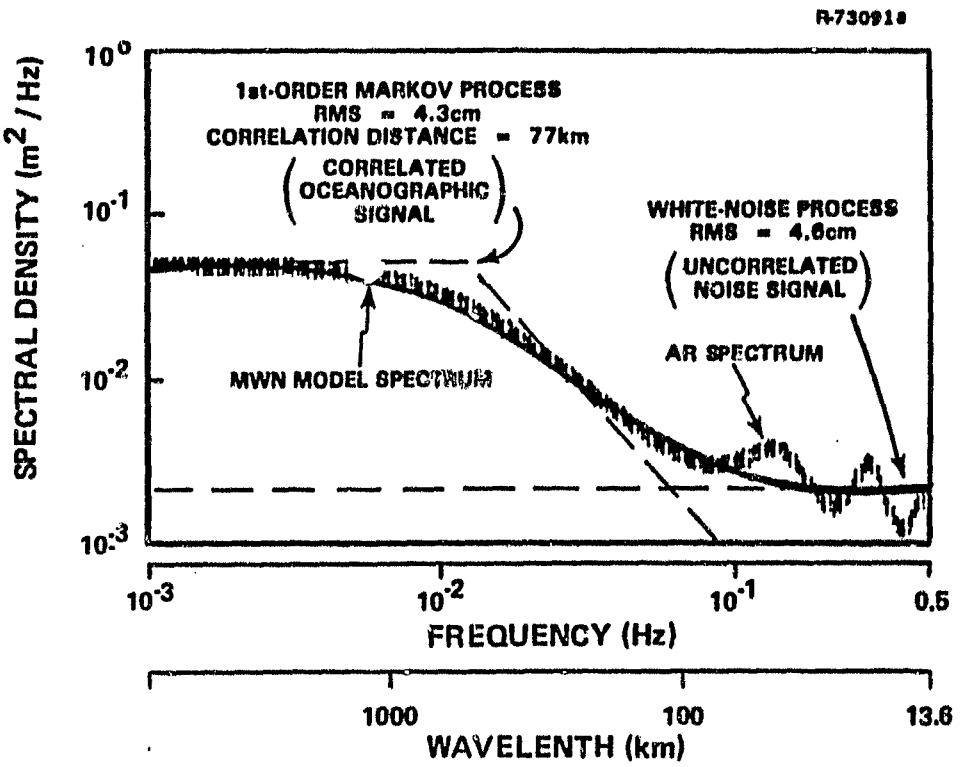

Figure 2.6-2 Power Spectra for Difference Data Along Rev. 1159D in North Atlantic

Such a model spectrum is shown as the smoothly varying solid curve in Fig. 2.6-2, labeled "MWN MODEL SPECTRUM". The asymptotes of this model spectrum are shown as dashed lines. The lower horizontal asymptote is the spectrum of the white-noise component alone. The sloping asymptote is the high-frequency trend of the Markov component in the absence of white noise. The sum of the Markov noise and the white noise has the smooth spectrum shape shown as the MWN (Markov plus White Noise) model in Fig. 2.6-2.

The corner frequency of 1.4×10^{-2} Hz marks the intersection of the low-frequency plateau and the sloping asymptote of the Markov spectrum. The wavelength of this corner frequency is 480 km.

With some tracks of data from the Gulf of Alaska, the low-frequency raised plateau is missing from the power spectrum because the Markov component is statistically insignificant; this situation is modeled by setting the variance of the Markov component equal to zero.

The white-noise component of the difference data is attributed to uncorrelated altimeter instrument noise plus microscale oceanography. The 1st-order Markov component, in contrast, is caused by a correlated signal that is attributed primarily to mesoscale time-varying oceanography. The Markov-plus-white-noise (MWN) model for the difference data is important because it provides quantitative information about the oceanographic information content of the altimeter data.

Data Model - The power spectrum of the MWN model has the following representation:

$$S(f) = \frac{\sigma_m^2 f_o/\pi}{f^2 + f_o^2} + S_{ww} \quad (m^2/Hz) \qquad (2.6\text{-}3)$$

where

σ_m = standard deviation of Markov component (m)

f_o = corner frequency (hz)

S_{ww} = spectral density of white noise (m^2/Hz)

The autocorrelation function of the Markov process is the inverse Fourier transform of the Markov spectral density

$$R_{mm}(t) = \int_{-\infty}^{\infty} \frac{\sigma_m^2 f_o/\pi}{f^2 + f_o^2} e^{i2\pi ft} dt \qquad (2.6\text{-}4)$$

$$R_{mm}(t) = \sigma_m^2 e^{-2\pi f_o |t|} \quad (m^2) \qquad (2.6\text{-}5)$$

where

t = time shift parameter (s)

The correlation time t_o of the Markov signal is defined as that value of the time shift for which $R_{mm}(t_o) = R_{mm}(0)/e$:

$$t_o = \frac{1}{2\pi f_o} \qquad (2.6\text{-}6)$$

The correlation distance d_o is computed by using the altimeter subtrack velocity v:

$$d_o = vt_o = \frac{v}{2\pi f_o} \qquad (2.6\text{-}7)$$

The variance of the white noise is computed for frequencies bounded by the folding frequency (half the data sampling frequency):

$$\sigma_w^2 = \int_{-f_s/2}^{f_s/2} S_{ww}\, df = S_{ww} f_s \qquad (2.6\text{-}8)$$

where

f_s = 1.0 Hz for 1-sample/second SEASAT data.

For Rev. 1159D in Fig. 2.6-2, the rms value of the Markov component is σ_m = 4.3 cm, the correlation distance is d_o = 77 km, and the rms value of the white noise is σ_w = 4.6 cm. The model parameters for all tracks of difference data are listed in Table 2.6-1 for the North Atlantic and in Table 2.6-2 for the Gulf of Alaska. The average rms value of the Markov component in the North Atlantic is 4.0 cm as compared to 1.8 cm in the Gulf of Alaska. There is less difference between the average rms values of the white noise components: 4.8 cm in the North Atlantic as compared to 3.8 in the Gulf of Alaska. These rms levels are consistent with a recent study of mesoscale oceanographic variability described in Ref. 4.

All of the analyzed repeat-track difference data were consistent with MWN models. As the data in Tables 2.6-1 and 2.6-2 indicate, the parameter values of the MWN models vary significantly from track to track in both the North-Atlantic and Gulf-of-Alaska regions. The variability of model parameters is depicted in Fig. 2.6-3, which shows the average of the spectrum aymptotes for the North-Atlantic data together with their minimum, maximum, and rms variations.

TABLE 2.6-1

MODEL PARAMETERS FOR REPEAT-TRACK DIFFERENCE DATA
NORTH ATLANTIC

REV. NO.	DAY	RMS OF MARKOV COMPONENT (cm)	CORRELATION DISTANCE (km)	RMS OF WHITE NOISE (cm)
1159D	0	4.3	77	4.6
1202D	3	3.5	52	3.1
1245D	6	4.9	137	5.4
1288D	9	5.5	10	7.4
1331D	12	2.6	15	4.0
1374D	15	2.9	49	3.3
1417D	18	3.6	28	5.4
1460D	21	4.4	21	5.1
Average Value		4.0	49	4.8
Standard Deviation		1.0	42	1.4
Maximum Value		5.5	137	7.4
Minimum Value		2.6	10	3.1

The observed variability indicates that the time-varying signals in repeat-track data are best modeled as non-stationary from track to track. Along single tracks the difference data are consistent with stationary models (for track lengths of 1300 km in the North Atlantic and 1000 km in the Gulf of Alaska). The parameter values of these stationary models sometimes change significantly over the three-day interval between successive repeat tracks.

TABLE 2.6-2

MODEL PARAMETERS FOR REPEAT-TRACK DIFFERENCE DATA
GULF OF ALASKA

REV. NO.	DAY	RMS OF MARKOV COMPONENT (cm)	CORRELATION DISTANCE (km)	RMS OF WHITE NOISE (cm)
1155A	0	2.6	21	4.7
1198A	3	3.3	30	3.9
1241A	6	0	NA	4.0
1284A	9	0	NA	3.0
1327A	12	1.9	69	3.1
1370A	15	2.4	7	2.2
1413A	18	1.6	44	2.9
1456A	21	0	NA	3.5
1499A	24	4.1	8	5.1
Average Value		1.8	30	3.6
Standard Deviation		1.5	24	0.9
Maximum Value		4.1	69	5.1
Minimum Value		0	7	2.2
NA = Not Applicable				

Kalman Smoothing - An important question bearing on the information content of the altimeter data is

- How accurately can the signal waveforms of the mesoscale components in the difference data be separated from the additive white noise?

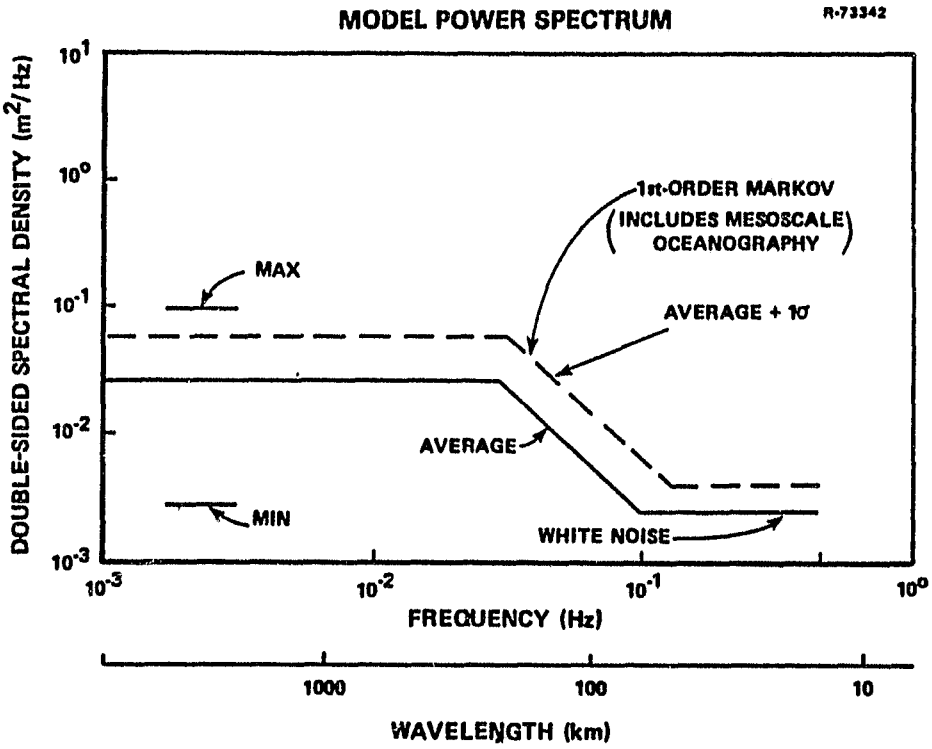

Figure 2.6-3 Summary of Model Power Spectra for Difference Data in North Atlantic

To answer this question, a Kalman fixed-interval smoother (Ref. 13) was designed for each track of difference data in the North Atlantic. Each smoother was optimal for estimating the mesoscale (Markov) waveform in a particular track of altimeter data. The waveform estimates were optimal in the sense that the estimation error variances were minimized, given the data model derived from AR analyses for each track of data.

The smoothed estimates of the mesoscale waveforms in the North-Atlantic data are shown in Fig. 2.6-4. Beside each waveform is the day number for the track and the rms error of the smoothed estimate as computed by the Kalman smoother for

that track. The theoretical rms errors of the estimates range from 1.3 cm to 2.5 cm, with an average of 1.9 cm. By comparing Fig. 2.6-1 (which shows the raw difference data for day 0) with the smoothed waveform at the top of Fig. 2.6-4, one sees how effectively the smoother suppresses the white noise in the data.

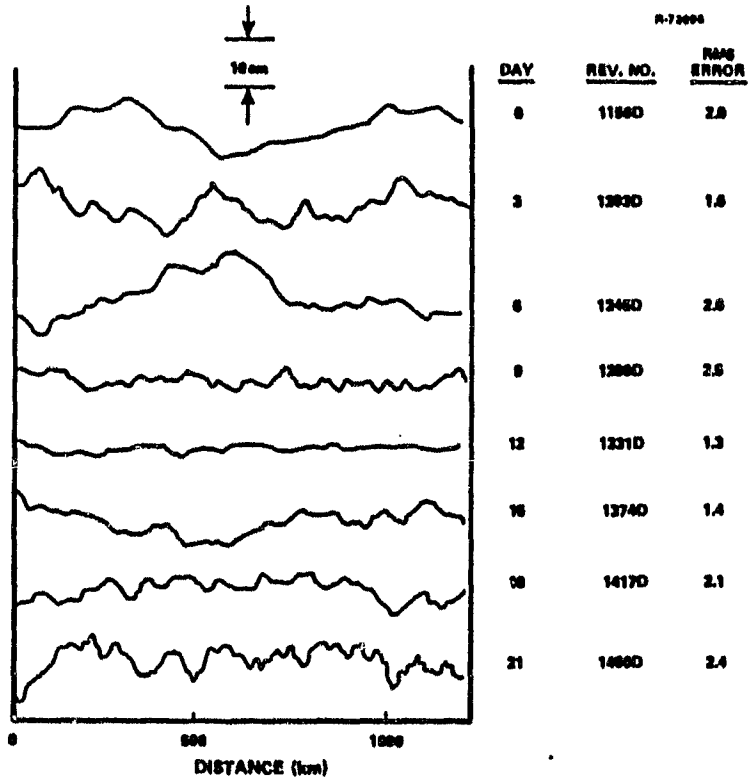

Figure 2.6-4 Smoothed Estimates of Time-Varying Mesoscale Signals in Repeat-Track Data from North Atlantic

The smoothed waveforms in Fig. 2.6-4 show statistically significant peak-to-peak differences from one track to the next. A good example of this variability is provided by the estimates for days 6, 9, and 12. The smoothed estimate for day 6 has a 19-cm peak-to-peak variation, while the day-9 and day-12 estimates are not significantly different from zero over most of their lengths.

2.7 TEMPORAL VARIABILITY OF GDR DATA CORRECTIONS

The estimated mesoscale waveforms in Fig. 2.6-4 may be affected by errors associated with the data corrections provided in the Geophysical Data Record (GDR) for the altimeter instrument and atmospheric effects. This potential error source was investigated by analyzing the sum of the GDR instrument corrections plus the atmospheric corrections for the set of repeat tracks in the North Atlantic.

The method of analysis followed the same pattern as the analysis of differenced altimeter data described earlier in this chapter. The analysis technique consisted of three steps:

- The time series of GDR corrections for all the repeat tracks were averaged to form an ensemble-mean time series for the set of eight tracks
- This ensemble-mean time series was subtracted from each track of correction data to form a time series of difference data for that track
- The power spectrum was estimated for each track of difference data (one for each repeat track) by subtracting a least-squares linear trend from each time series and then using the autoregressive (AR) modeling technique described in Section 2.4.

The difference data contain the time-varying components of the correction signals, and the power spectra measure the distribution of power in these signals as a function of frequency. The rms magnitudes of the time-varying correction signals varied from track to track: the minimum was 0.2 cm; the maximum was 1.6 cm; and the mean was 0.8 cm. The standard deviation about the mean was 0.4 cm. These rms magnitudes are

small compared to the rms values found for the time-varying mesoscale signals in the sea surface height data.

The estimated power spectra for the time-varying correction signals were compared with the corresponding spectra for the time-varying signals in the sea-surface height (SSH) data. The comparison showed that the time-varying SSH data typically have more than ten times the power of the time-varying correction data for wavelengths shorter than 1000 km.

If the assumption is made that the errors in the GDR corrections for instrument and atmospheric effects are smaller than the corrections themselves, then the analysis of the correction data supports the following conclusion: in the nearly repeating tracks of altimeter data used for this study, the instrument and atmospheric effects are significantly smaller than the observed temporal variability.

2.8 CONCLUSIONS ON INFORMATION CONTENT

Based on the analyses of North-Pacific and North-Atlantic residual SEASAT altimeter data, the following conclusions are reached:

- Residual altimeter data have the statistical properties of correlated Gaussian random noise
- Residual data are statistically modeled as the sum of white (uncorrelated) noise plus a Markov (mesoscale) process
- Mesoscale signal components in the residual data are attributed primarily to geoid estimation errors and mean sea-surface height signatures

- Each track of repeat-track difference data has the statistical properties of a Gaussian process consisting of white noise plus a mesoscale 1st-order Markov process. The rms values of the white and mesoscale signal components often vary significantly over 3-day intervals within each set of repeat tracks. The average rms values of these signal components (and sample standard deviation σ of the rms values) are listed for the two study regions:

  RMS WHITE-NOISE LEVELS
  North Atlantic: 4.8 cm (σ = 1.4 cm)
  Gulf of Alaska: 3.6 cm (σ = 0.9 cm)

  RMS MESOSCALE SIGNAL LEVELS
  North Atlantic: 4.0 cm (σ = 1.0 cm)
  Gulf of Alaska: 1.8 cm (σ = 1.5 cm)

- Kalman smoothers for the difference data provide minimum-variance estimates of the time-varying mesoscale signal waveforms. The nonstationary data require a unique smoother for each repeat track, and the rms estimation accuracy varies from track to track. Average rms estimation accuracy for North-Atlantic data is 1.9 cm.

- The mean-square temporal variability of instrumental and atmospheric corrections for the altimeter data (Sept. 1980 GDR tape) is less than 10 percent of the variability in the difference data for wavelengths < 1000 km.

2.9 QUESTIONS FOR FURTHER STUDY

The results of this study raise the following questions for future study:

- How much of the observed mesoscale variability in the repeat-track difference

data is correlated with variations in the significant wave height on the GDR tape?

- If there is significant correlation, how does it vary with wavelength?

The answers to these questions may be found on a track-by-track basis via multi-channel AR modeling techniques for estimating spectral coherence.

3. OCEAN-CURRENT DETECTION ALGORITHM

3.1 INTRODUCTION

Approach - The approach to developing an automatic algorithm for detecting specific ocean-current signatures in single tracks of altimeter data is based on the results of the study of the oceanographic information content of SEASAT data in Chapter 2. The approach consists of three steps:

- The residual altimeter data are modeled as samples of Gauss-Markov noise plus the possible occurrences of specific ocean-current signatures (boundary currents, cold-core rings, etc)
- The correlation structure of the noisy signal components in the data are identified for each track of data with a data-adaptive AR modeling algorithm
- The hypotheses that specific current signatures are present in the data are tested by using optimal matched filters and threshold detectors.

Algorithm Structure - The ocean-current detection algorithm processes single tracks of residual satellite altimeter data and yields the following outputs:

- Detected locations of specified ocean-current signatures along the satellite subtrack
- Estimated amplitudes of the detected signatures

- Estimated rms errors for the locations and amplitudes of detected signatures
- Expected number of false alarms.

The residual altimeter data are inputs to the algorithms and are computed from raw altimeter data in three steps by

- Applying corrections for known error sources
- Interpolating the data through intervals in which the data are in serious error (e.g., outliers)
- Subtracting an estimated gravimetric geoid profile along the satellite subtrack.

The resulting residual data are noisy measurements of the dynamic sea-surface height. The characteristics of the noise in these data depend on the noise in the raw altimeter data and on the accuracies of the error corrections and the geoid profiles. The detection algorithm exploits both the statistical properties of the noise in the residual data and the known average properties of ocean-current signatures in the altimeter data. For specified models of the noise and oceanographic signature, the algorithm maximizes the probability of detection at a specified probability of false alarm and minimizes the rms errors of the estimated current signature parameters.

As depicted in Fig. 3.1-1, the detection algorithm consists of four subalgorithms that perform separate functions.

- AUTOREGRESSIVE MODELING - The residual data are analyzed to determine a stochastic autoregressive (AR) model for

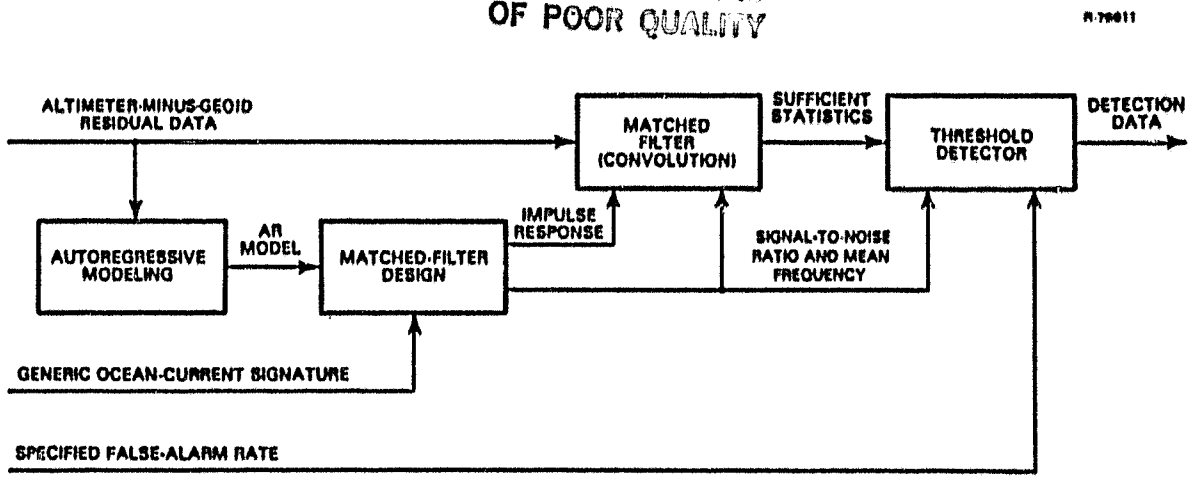

Figure 3.1-1 Structure of Data-Adaptive Current Detection Algorithm

the process that generated the data. The order of the AR model is selected to minimize the Akaike information criterion (AIC).

- MATCHED-FILTER DESIGN - The AR model, together with a user-specified generic ocean-current signature, are used to compute the impulse response of the optimal matched filter for detecting and locating the generic signature in the noisy residual data.

- MATCHED FILTER - The impulse response of the matched filter is convolved with the residual altimeter data to compute a sequence of sufficient statistics for the threshold detector.

- THRESHOLD DETECTOR - The detector compares the sufficient statistics with a threshold value that is chosen to yield a specified false-alarm rate. A detection occurs when the statistic exceeds the threshold. The estimated location of the detected signature is given by the location of the local maximum of the statistic.

Overview - This chapter describes the development and verification of the detection algorithm. Section 3.2 describes the SEASAT data selected for the verification of the algorithm. Generic ocean-current signature models are presented in Section 3.3. The results of processing SEASAT data to detect the Gulf Stream and cold-core ring currents in the western North Atlantic are discussed in Sections 3.4 and 3.5. After discussing the verification results in Section 3.6, the mathematical basis of matched-filter detection is discussed in Sections 3.7 and 3.8. Algorithm performance is discussed in Sections 3.9 and 3.10. The chapter concludes with a summary in Section 3.11 and a discussion of areas for future study in Section 3.12.

3.2 DATA SELECTED FOR DEMONSTRATING CURRENT-DETECTION ALGORITHM

Four tracks of SEASAT altimeter data from the western North Atlantic were selected to verify the performance of the detection algorithm. The tracks are Revs. 234A, 277A, 478A, and 572D. These tracks crossed cold ring No. 4 as depicted in Fig. 3.2-1. The motion of this ring current had been tracked using a variety of oceanographic data (Ref. 6). These four tracks also intersected the Gulf Stream and therefore provided data to verify the algorithm performance with respect to the detection of both boundary currents and eddy currents.

The tracks of data used to verify the algorithm extend beyond the latitude limits shown in Fig. 3.2-1; the test data extend from 25 deg to 39 deg north latitude.

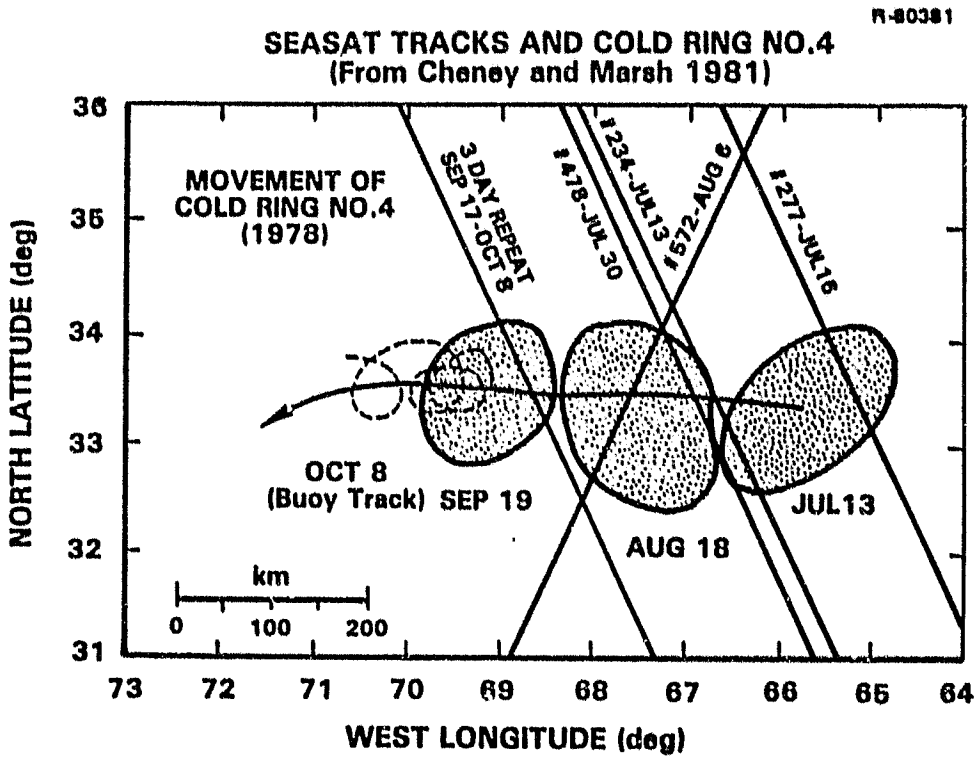

Figure 3.2-1 Selected Data for Demonstrating Current-Detection Algorithm

3.3 GENERIC OCEAN-CURRENT SIGNATURE MODELS

This section describes two parametric families of ocean-current signatures. The first family is used for designing matched filters to detect warm-core and cold-core current rings. The second family is intended for detecting boundary currents, such as the Gulf Stream, and for estimating geostrophic current velocities.

Ring-Current Signatures - A family of generic altimetric signatures is described for modeling the dynamic sea-surface features caused by cold-core and warm-core current rings. The sea-surface height H(x) at radial position x with respect to the ring's center is modeled as

$$H(x) = - D \exp (-9.21 (x/W)^2) \qquad (3.3\text{-}1)$$

D = signature depth

W = signature width (10 percent depth)

D is positive for cold rings and negative for warm rings. This parametric model has a simple mathematical form and appears to be in reasonable agreement with available data on ring signatures (e.g., Refs. 6-8).

The width W is defined as the diameter at which the signature is 10 percent of its central value:

$$H(W/2) = H(0)/10 \qquad (3.3\text{-}2)$$

Equation 3.3-1 has the form of a Gaussian probability density. Therefore, these are referred to as Gaussian ring signatures. An example of a Gaussian ring signature is shown in Fig. 3.3-1, where the central depth is 0.5 meter and the width is 150 km.

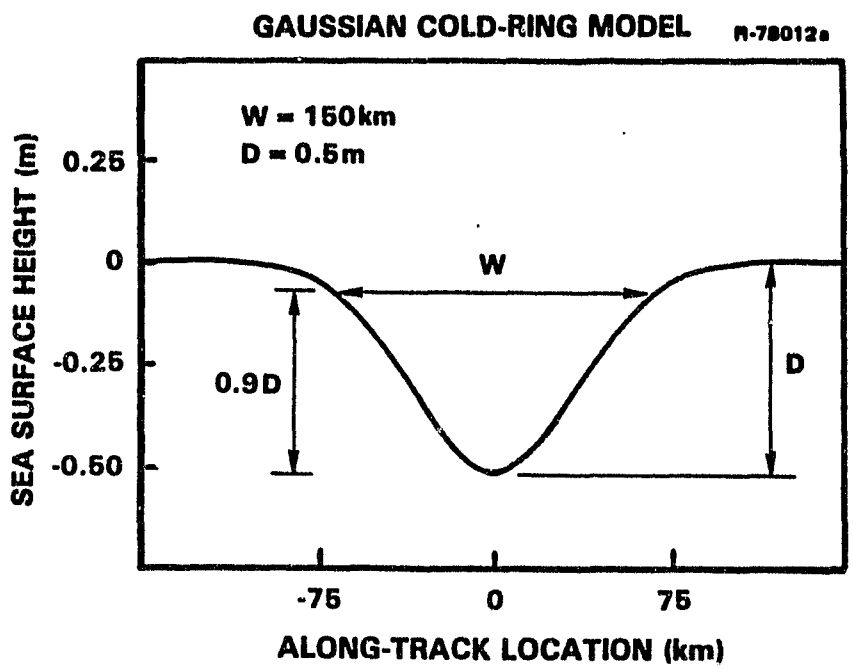

Figure 3.3-1 Gaussian Cold-Ring Signature, Depth = 0.5 m, Width = 150 km

The tangential current-velocity distribution implied by a ring signature may be computed by setting the radial slope of the sea surface equal to the sum of the horizontal Coriolis acceleration and the centrifugal acceleration divided by the acceleration of gravity:

$$\frac{dH(x)}{dx} = \frac{f\ v(x) + v^2(x)/x}{g} \qquad (3.3\text{-}3)$$

$f = 2\Omega \sin\phi$ = Coriolis parameter

Ω = earth's rotational velocity

ϕ = latitude

$v(x)$ = tangential current velocity

g = acceleration of gravity.

The geostrophic velocity component is

$$V_g(x) = \frac{g}{f} \frac{dH(x)}{dx} \qquad (3.3\text{-}4)$$

Solving Eq. 3.3-3 for the total current velocity v(x) yields

$$v(x) = \frac{x\ f}{2} \left[\sqrt{1 + \frac{4V_g(x)}{x\ f}} - 1 \right] \qquad (3.3\text{-}5)$$

For a Gaussian 0.5-m 150-km ring signature at 45-degrees latitude, Eqs. 3.3-4 and 3.3-5 yield the velocity distributions shown in Fig. 3.3-2. The geostrophic approximation is seen to over-estimate the maximum velocity by approximately 0.1 m/s (18 percent).

Boundary Current Signatures - A family of generic altimetric signatures for boundary currents is defined with

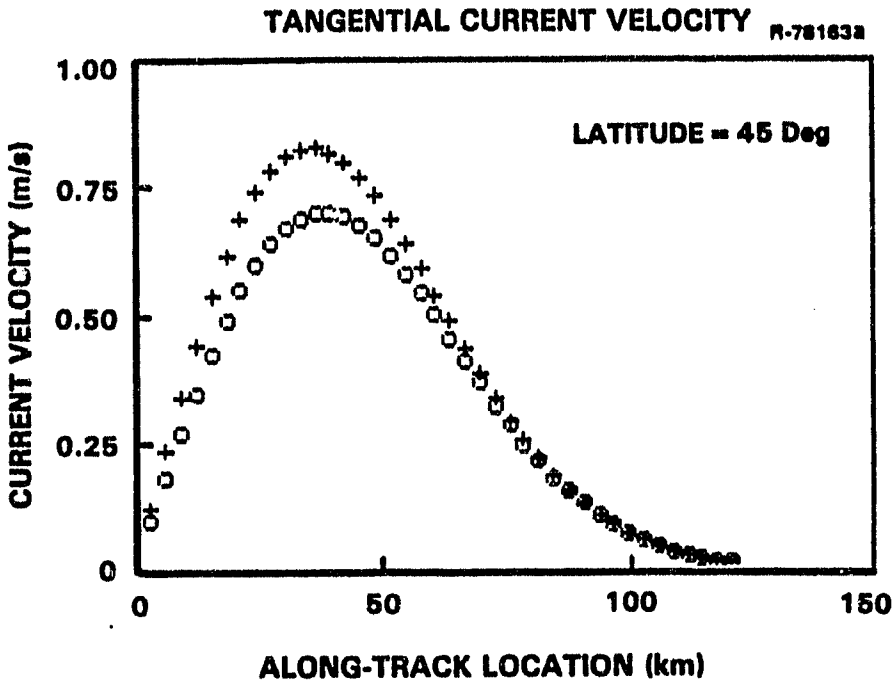

Figure 3.3-2 Tangential Current-Velocity Distributions in Gaussian Cold Ring. Crosses = geostrophic approximation; circles = geostrophic approximation with centrifugal correction.

the aid of Fig. 3.3-3, which depicts a satellite subtrack crossing a current at angle θ. At position x along the subtrack, the dynamic height H(x) is modeled with the hyperbolic tangent function:

$$H(x) = -(A/2)\ \tanh(3\ x\ \sin\theta/W_c) \qquad (3.3\text{-}6)$$

A = amplitude of dynamic height change

θ = track angle with respect to current velocity

W_c = width of current (90 percent height change)

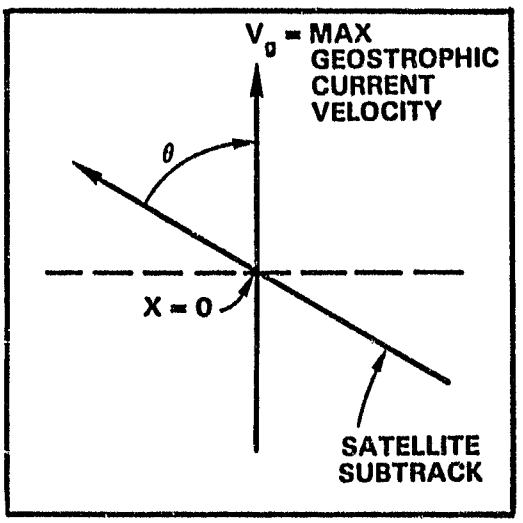

Figure 3.3-3 Geometry of Geostrophic Current and Satellite Subtrack

As shown in Fig. 3.3-4, the tanh model signature provides a reasonable fit to the SEASAT altimeter data for Rev. 234A where the subtrack crosses the Gulf Stream centered at sample number 233. The tanh model provides similar fits to other tracks of SEASAT data; further examples are discussed in Section 4.3.

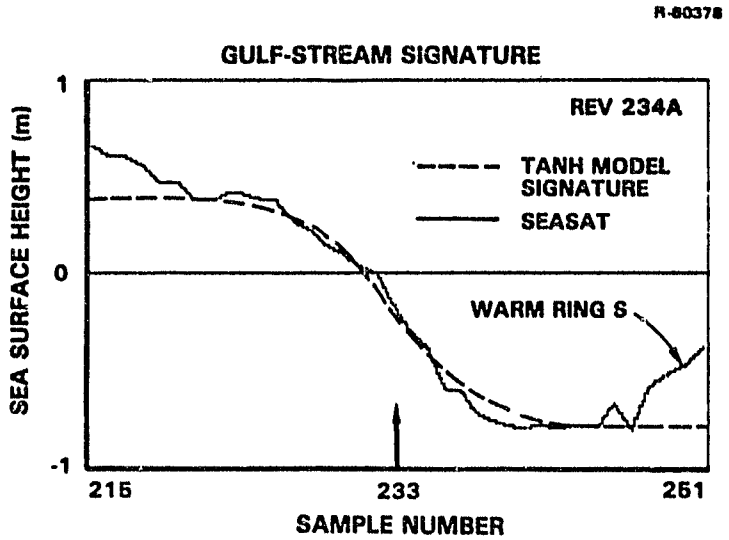

Figure 3.3-4 Comparison of Tanh Model Signature with SEASAT Data Rev. 234A

The along-track slope of the tanh signature is

$$\frac{dH(x)}{dx} = - \frac{3\ A\ \sin\theta}{2\ W_c} \operatorname{sech}^2\left[\frac{3\ x\ \sin\theta}{W_c}\right] \qquad (3.3\text{-}7)$$

For the coordinate system in Fig. 3.3-3, this slope is related to the cross-track component $V_c(x)$ of the geostrophic velocity as follows

$$V_c(x) = - \frac{g}{f} \frac{dH(x)}{dx} \qquad (3.3\text{-}8)$$

For tracks that cut across the current, the geostrophic velocity profile $V_g(x)$ along the subtrack is proportional to the cross-track velocity $V_c(x)$

$$V_g(x) = V_c(x)/\sin\theta \qquad (3.3\text{-}9)$$

For the signature slope given by Eq. 3.3-7, the geostrophic velocity profile is therefore

$$V_g(x) = \frac{3\ A\ g}{2\ f\ W_c} \operatorname{sech}^2\left[\frac{3\ x\ \sin\theta}{W_c}\right] \qquad (3.3\text{-}10)$$

The signature amplitude parameter A is proportional to the maximum geostrophic velocity $V_g(0)$

$$A = \frac{2\ f\ W_c}{3\ g} V_g(0) \qquad (3.3\text{-}11)$$

For tracks that intersect the current, the signature width W_s is proportional to the current width W_c

$$W_s = W_c/\sin\theta \qquad (3.3\text{-}12)$$

Typical model parameters for the Gulf Stream in the western North Atlantic are an amplitude of A = 1 m, a maximum geostrophic velocity of $V_g(0)$ = 2 m/s, and a latitude of ϕ = 45 deg. From Eq. 3.3-11 the current's width is W_c = 71 km. For a nominal track crossing angle of 60 deg, the along-track width of the signature is W_s = 82 km. Figure 3.3-5 shows the dynamic sea-surface height signature for these parameter values, while Fig. 3.3-6 depicts the geostrophic velocity profile implied by the height signature.

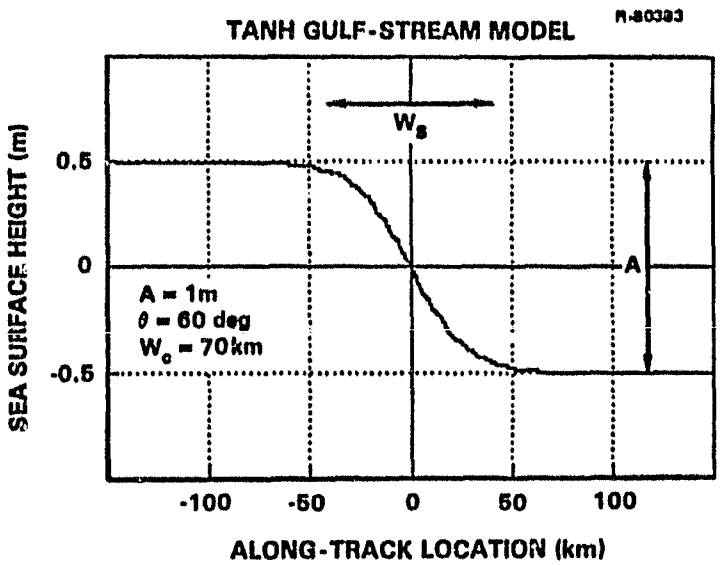

Figure 3.3-5 Dynamic Sea-Surface Height Signature

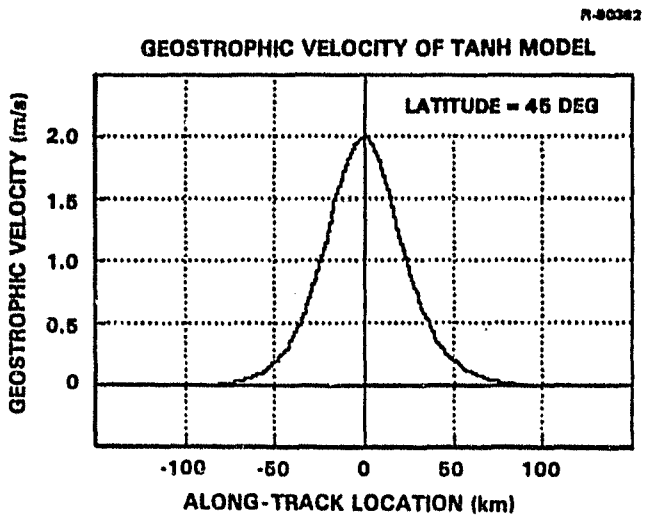

Figure 3.3-6 Geostrophic Velocity Profile

3.4 DEMONSTRATIONS OF GULF-STREAM DETECTION

This section presents four examples of using the algorithm (Section 3.1) to detect automatically the Gulf-Stream signature in SEASAT data from which Marsh-Chang geoid estimates (Ref. 14) were subtracted. The tanh model signature (Eq. 3.3-6 with $W_s = W_c/\sin\theta$) was used with the signature width W_s ranging from 35 km to 150 km.

Example 1 - As depicted in Fig. 3.4-1, the residual SEASAT data for Rev. 572D are used as input to the detection algorithm. The algorithm is optimized in this example for the tanh model signature having a width of 60 km. The scaled output of the matched-filter is shown with the detection threshold chosen for a false-alarm rate (FAR) of 0.01 false alarm per megameter of track length (A/Mm).

The filter output is seen to rise above the threshold and reach a local maximum at data sample number 64. This is a correct detection of the Gulf Stream. There are no other crossings of the threshold, which means that there are no false alarms. The algorithm successfully discriminates against the signature in the altimeter data due to cold ring number 4.

Figure 3.4-2 shows the same input data for Rev. 572D along with the resulting scaled outputs of three matched filters. Each filter is optimized for a different signature width (40 km, 60 km, and 150 km). All filters correctly detect the Gulf Stream with no false alarms, which demonstrates that the algorithm performance is insensitive to the choice of model signatures. The detection threshold in each case is chosen to yield FAR = 0.01 A/Mm. The 60-km filter produces the largest Gulf-Stream response, and for that reason its estimate of the current's location (sample number 64) is the most likely of the three estimates available. The theoretical basis for using

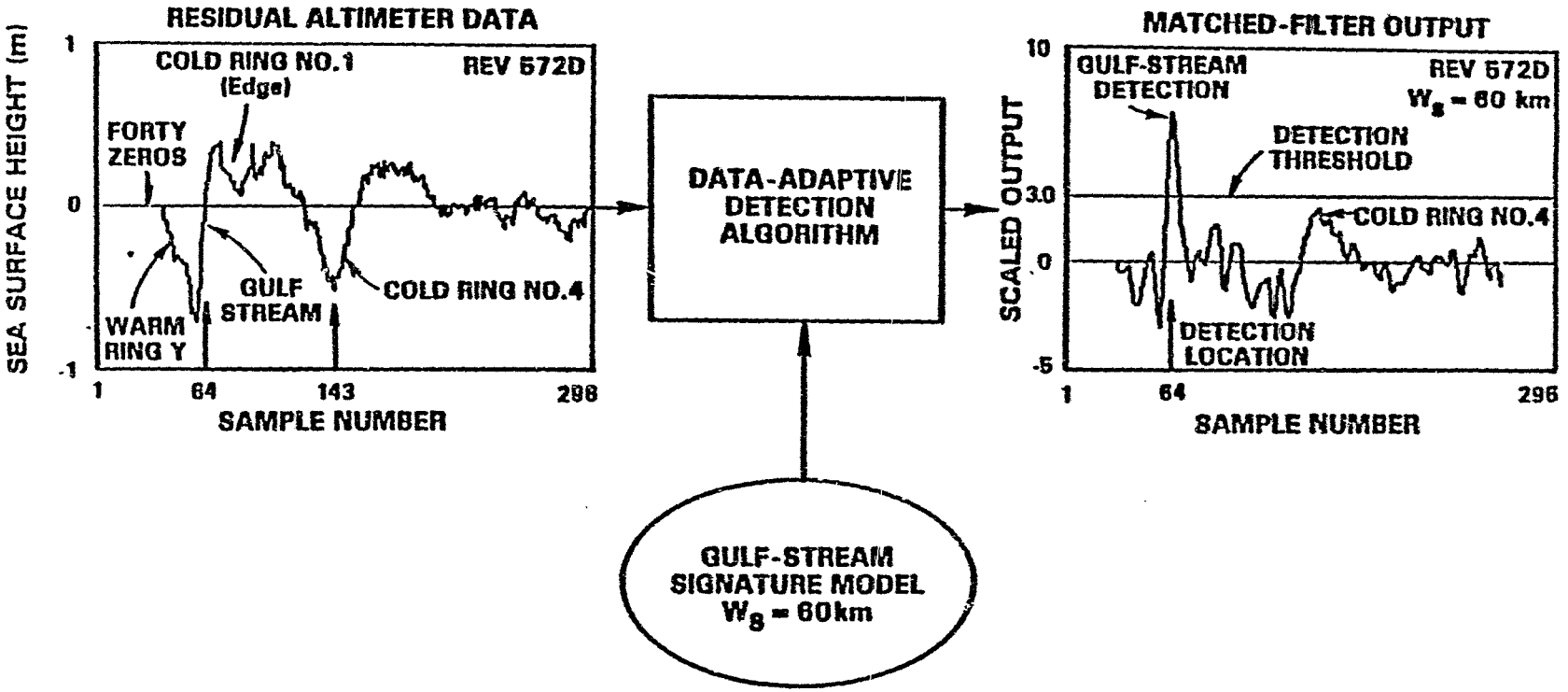

Figure 3.4-1 Demonstration of Gulf-Stream Detection Using SEASAT Data Rev. 572D

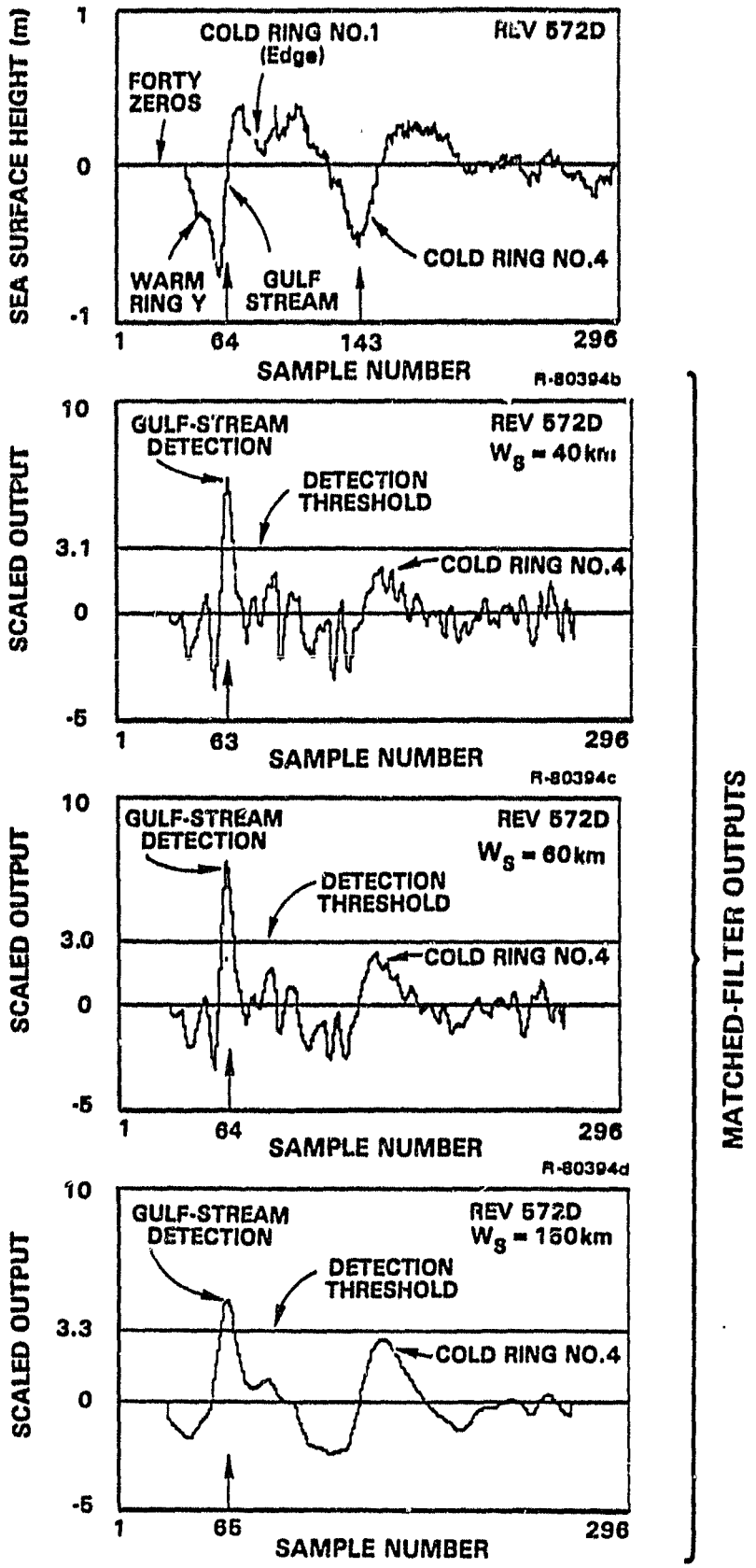

Figure 3.4-2 Rev. 572D Gulf-Stream Detection

the filter that produces the largest scaled output is explained in Section 3.7. The autoregressive (AR) model for the data is computed by the detection algorithm operating on the last 230 samples of the altimeter data; this avoids Gulf-Stream bias in the modeling of the background noise in the altimeter data.

The output of each matched filter is scaled so that the random noise in the output signal has a standard deviation of unity. Therefore, the detection threshold of the 60-km filter, which is labeled 3.0, corresponds to an output level that is three sigmas (three standard deviations) away from the mean. The three filters differ in their dynamics, as indicated by the smoother output waveforms from the filters optimized for the wider signatures. Because of these differing dynamics, the fixed false-alarm rate leads to slightly different detection thresholds (when expressed in standard deviations) for the three filters.

Example 2 - Figure 3.4-3 depicts the results of processing the residual SEASAT data for Rev. 478A with three matched filters optimized for widths of 35 km, 100 km, and 150 km; the detection thresholds are chosen to yield FAR = 0.01 A/Mm. In this example, the Gulf Stream is located at the right end of the data set because Rev. 478A is an ascending track in which the Gulf Stream occurs at the end of the time series. All three filters are successful in detecting the Gulf Stream, and there are no false alarms. The AR model for the data is generated by the algorithm using the first 215 samples of data to avoid the Gulf-Stream signature. Experience shows that the algorithm performs well even if the Gulf-Stream signature is included in the data used to develop the AR model. The primary consequence of using all the data for AR modeling is that the detection thresholds are moved to slightly higher values, because

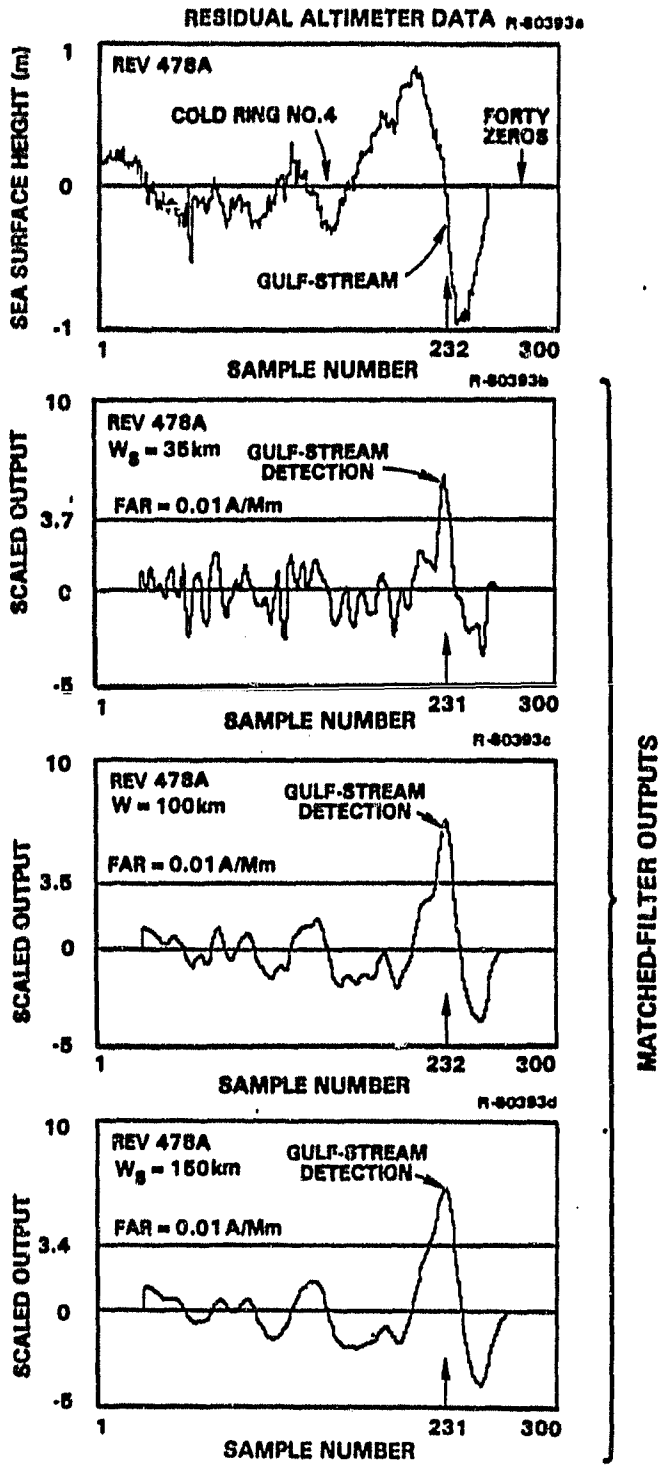

Figure 3.4-3 Demonstration of Gulf-Stream Detection SEASAT Rev. 478A

the algorithm then underestimates the ease with which the Gulf-Stream signature can be detected.

Example 3 - Figure 3.4-4 is an example of Gulf-Stream detection using Rev. 277A. This Rev. is interesting because it contains erroneous data caused by the island of Bermuda. The outputs of two matched filters are shown, one matched to a narrow 35-km signature and the other matched to a 60-km signature; these filters use an AR noise model based on the first 225 data samples. Both filters correctly detect the Gulf Stream, and there are no false alarms. The data errors due to Bermuda cause a relatively large response from the narrow 35-km filter, which is the more sensitive filter to narrow waveforms in the data. This example illustrates that the 60-km matched-filter detector is robust against naturally occurring localized data errors.

Example 4 - This last example uses SEASAT data from Rev. 234A as shown in Fig. 3.4-5. The data set contains an isolated data error and the edge of a warm-ring signature. The scaled outputs of two matched filters are shown with detection thresholds corresponding to FAR = 0.01 A/Mm. The filters are matched to signature widths of 35 km and 100 km, and the AR noise model is based on the first 225 data. Both filters correctly detect the Gulf Stream without any false alarms. The data error causes a relatively large output from the 35-km filter, but has little effect on the output of the 100-km filter. Both filters discriminate well against the signature of warm ring S.

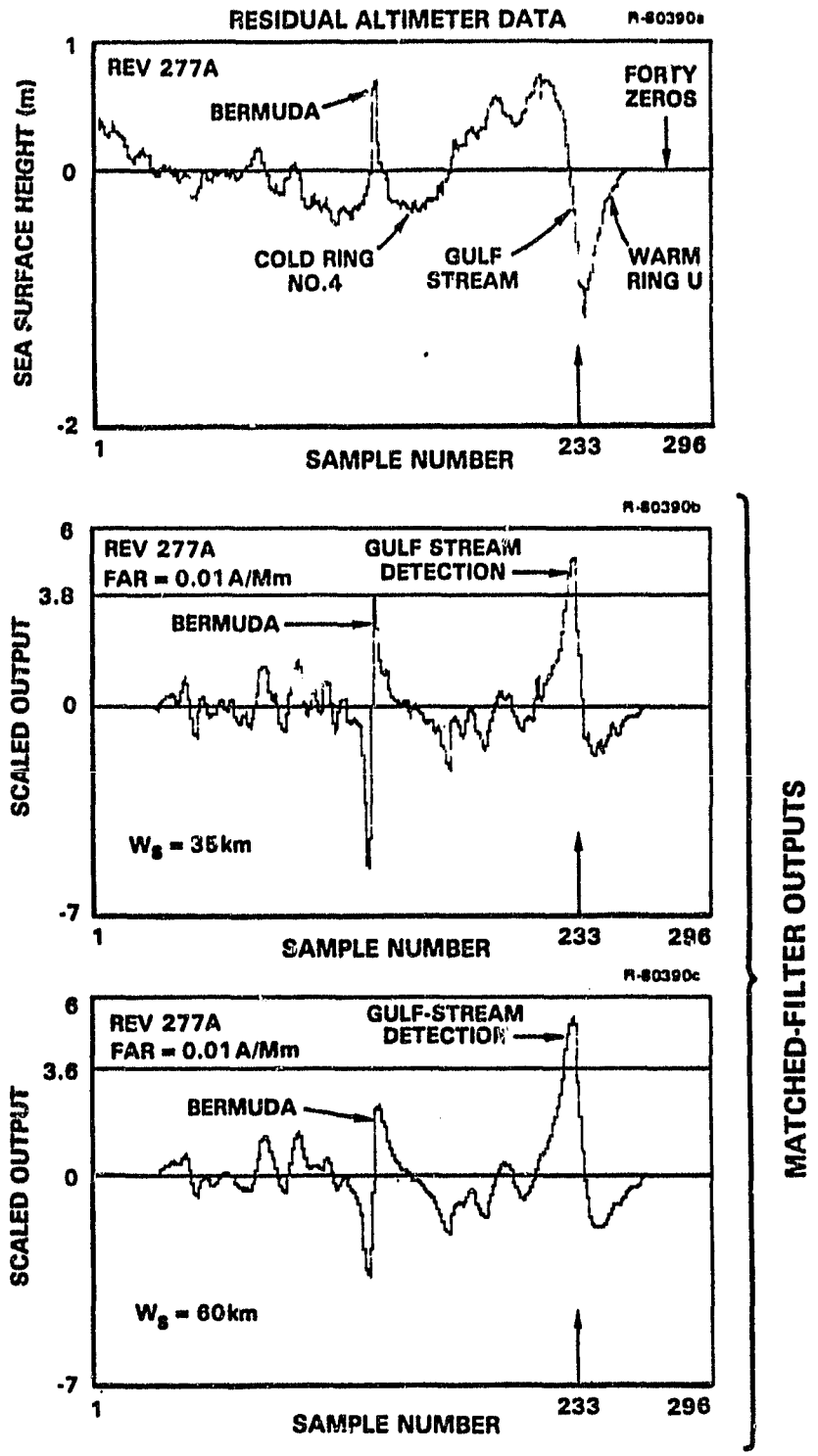

Figure 3.4-4 Demonstration of Gulf-Stream Detection SEASAT Rev. 277A

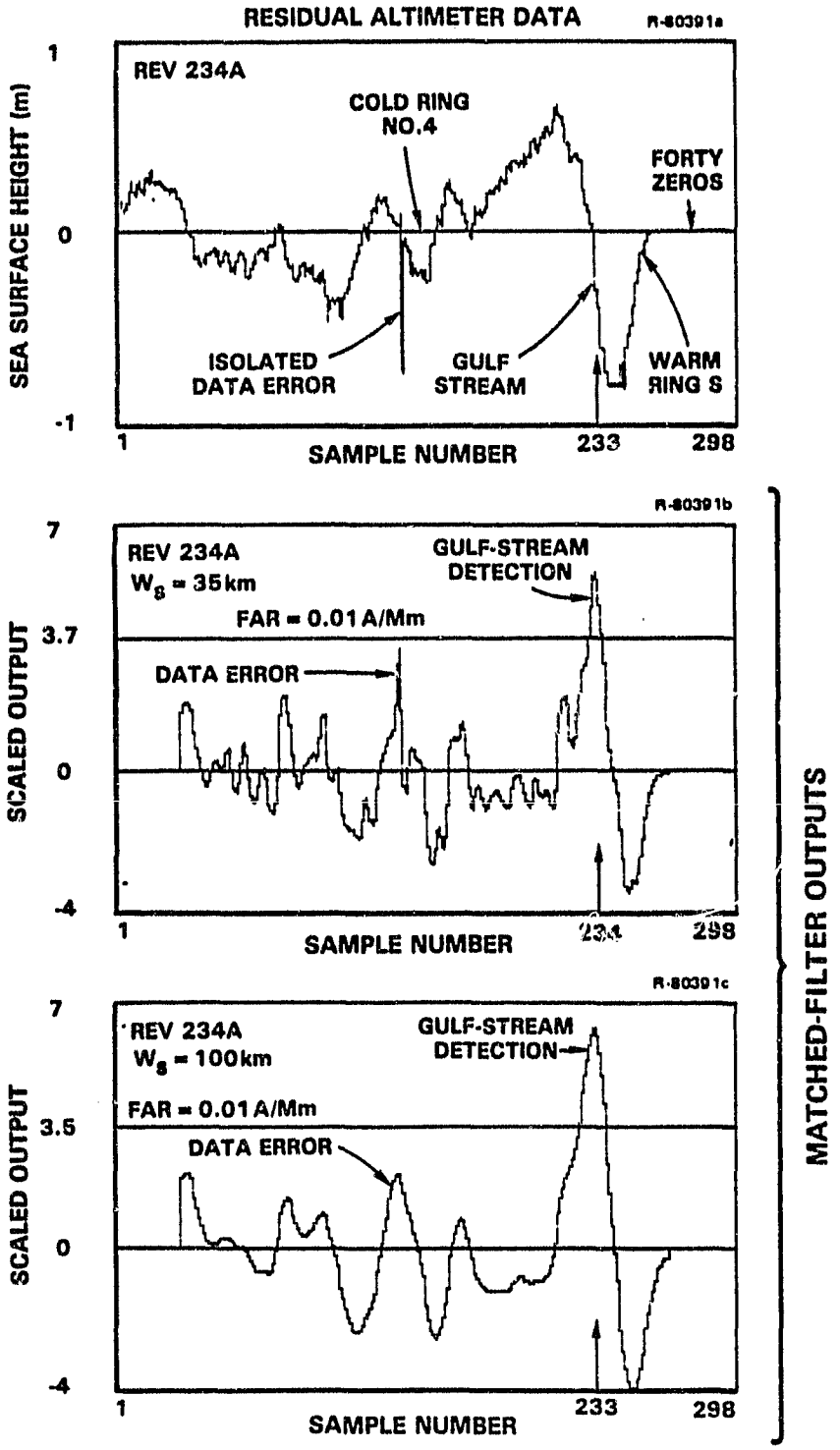

Figure 3.4-5 Demonstration of Gulf-Stream Detection SEASAT Rev. 234A

3.5 DEMONSTRATIONS OF COLD-RING DETECTION

This section presents four examples of using the detection algorithm to detect automatically the signatures of cold ring number 4 in SEASAT data from which Marsh-Chang geoid estimates (Ref. 14) were subtracted. The data sets used here are the same as the ones used in Section 3.4. The Gaussian model signature (Eq. 3.3-1) is used in the algorithm with two values for the signature width: 150 km and 300 km.

Example 1 - Figure 3.5-1 shows the SEASAT data for Rev. 572D and the outputs of two matched filters. The algorithm designed these filters for signature widths of 150 km and 300 km by using an AR noise model based on the last 230 data (to avoid the Gulf-Stream signature). The detection thresholds correspond to FAR = 0.1 A/Mm. This false-alarm rate is ten times larger than the value used in Section 3.4 for Gulf-Stream detection. The larger FAR is used in this example because cold-ring signatures are more difficult to detect than boundary-current signatures; the ring signatures are more difficult to discriminate against the ambient noise signals in the data.

Cold ring number 4 is correctly detected by the 300-km filter. The 150-km filter misses the ring because the model signature is too narrow. Both filters produce false alarms due to the Gulf Stream, but these are the only false alarms. Experience shows that the Gulf Stream consistently causes false alarms when the algorithm is attempting to detect cold rings. The conclusion to be reached is that the data must be processed in two passes. The first pass is used to detect the possible occurrence of boundary-current signatures. If a boundary-current signature is detected, then the data set is truncated to exclude the detected current during the second pass. The second pass is then used to detect the possible occurrence of

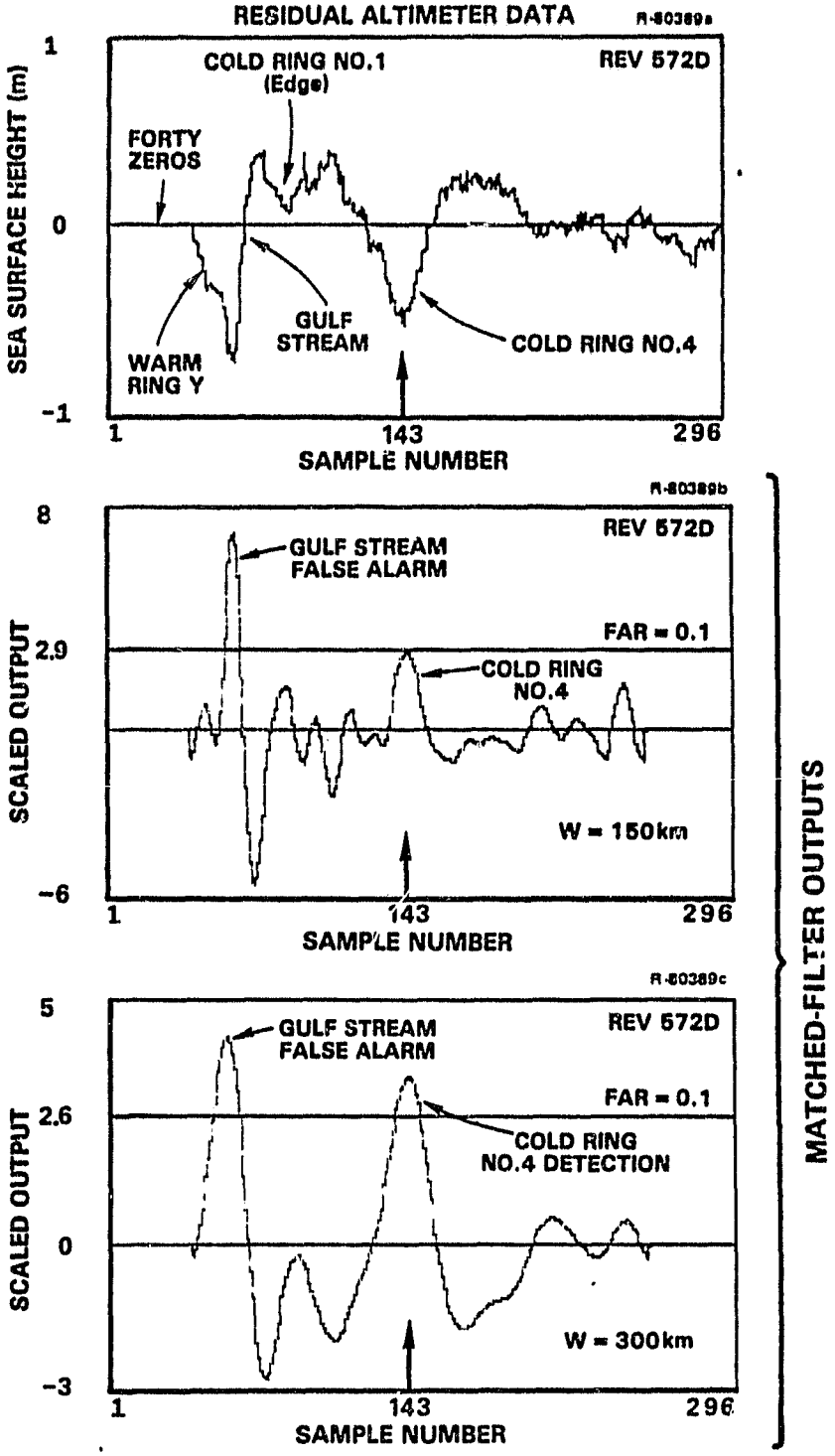

Figure 3.5-1 Demonstration of Cold-Ring Detection
SEASAT Rev. 572D

eddy currents. This strategy requires a small amount of computation (0.5 sec per pass using an IBM 4341 computer) and prevents false alarms due to boundary currents. This two-pass technique is used in the following examples.

Example 2 - Figure 3.5-2 shows SEASAT data from Rev. 478A, which are used as input for two filters matched to signatures having widths of 150 km and 300 km. The algorithm implemented these filters using an AR model based on the first 140 data. This selective use of data leads to the most accurate detection thresholds to achieve a specified false-alarm rate. When the algorithm uses all the data to compute the AR noise model (as it likely would in operational data analysis), the detection thresholds are raised slightly because the algorithm then overestimates the likelihood of false alarms.

The 300-km filter correctly detects cold ring number 4 at a false-alarm rate of 0.03 A/Mm. In contrast, the 150-km filter misses the ring even with the larger FAR of 0.1 A/Mm, which demonstrates the ability of the algorithm to discriminate between narrower and wider current signatures. There are no false alarms.

Example 3 - Figure 3.5-3 shows the SEASAT data from Rev. 277A, which contains data errors caused by the island of Bermuda and a signature due to cold ring number 4. The data are processed by two filters matched to cold-ring signatures having widths of 150 km and 300 km. The algorithm implemented the filters using an AR noise model based on the first 134 data to avoid any bias from the Bermuda signature. The 300-km filter correctly detects cold ring number 4 at a false-alarm rate of 0.2 A/Mm. The depression in the altimeter data to the left of Bermuda also causes an alarm in the output. This may be a false alarm; no data are available for certifying the origin of the signature. The 150-km filter misses cold ring number 4.

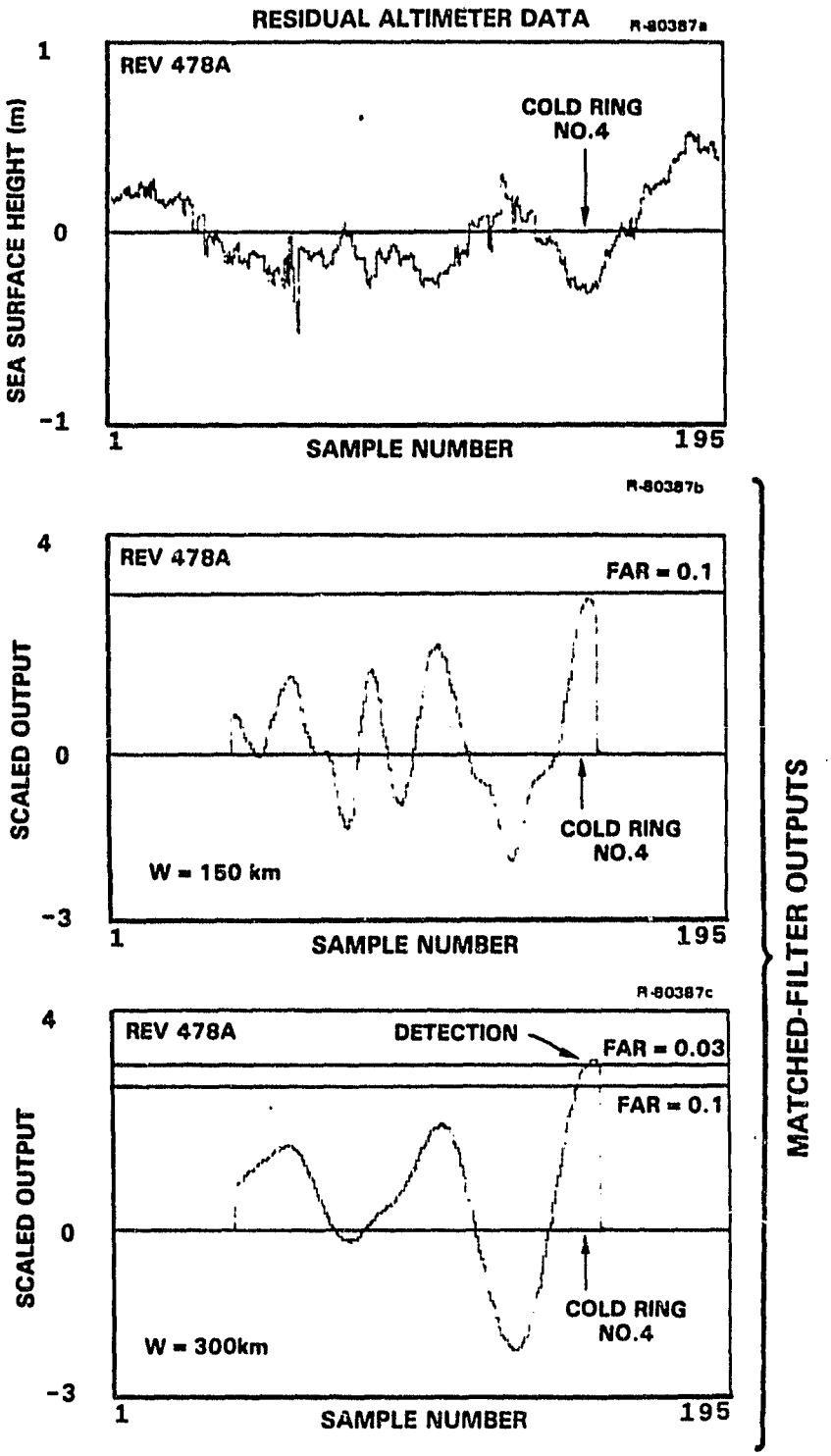

Figure 3.5-2 Demonstration of Cold-Ring Detection SEASAT Rev. 478A

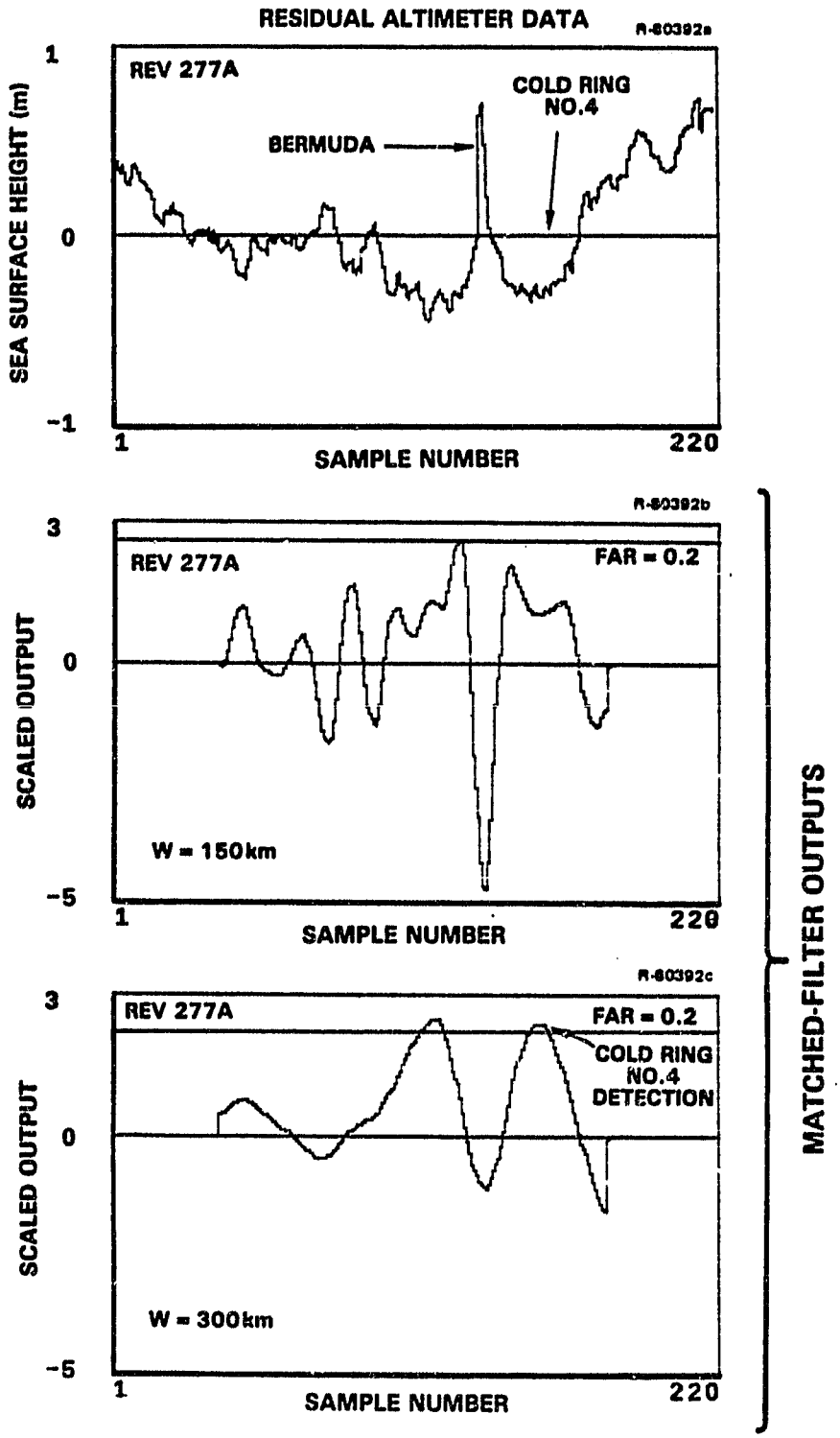

Figure 3.5-3 Demonstration of Cold-Ring Detection SEASAT Rev. 277A

Example 4 - Figure 3.5-4 shows the SEASAT data from Rev. 234A; the isolated data error has been corrected by simple interpolation. The edge of cold ring number 4 is visible and spans approximately 200 km in the data. To detect this signature, the data are processed twice with the detection algorithm, once to implement a detection filter matched to a signature width of 150 km, and again for a filter matched to a width of 300 km. For this example, the algorithm uses all 220 data in computing the AR noise model.

The scaled outputs of the filters show that the cold ring is correctly detected by both filters at a false-alarm rate of 0.5 A/Mm. There are no false alarms with the 150-km filter. Whether the alarm in the middle of the 300-km filter output is false cannot be certified because surface truth data are not available.

3.6 DISCUSSION OF DEMONSTRATION RESULTS

The verifications of algorithm performance described in Sections 3.4 and 3.5 lead to several conclusions:

- The required computing time is modest: less than 0.5 sec per track for a one-signature (one-filter) analysis using an IBM 4341 computer
- The Gulf Stream is easily detected at a low false-alarm rate: a single model signature is adequate; and FAR < 0.01 A/Mm
- Cold rings are detected with some risk of false alarms. Processing the altimetry with two or three filters (to search for two or three model signatures) increases the likelihood of detection for a specified false-alarm rate. The detection of cold ring number 4 typically

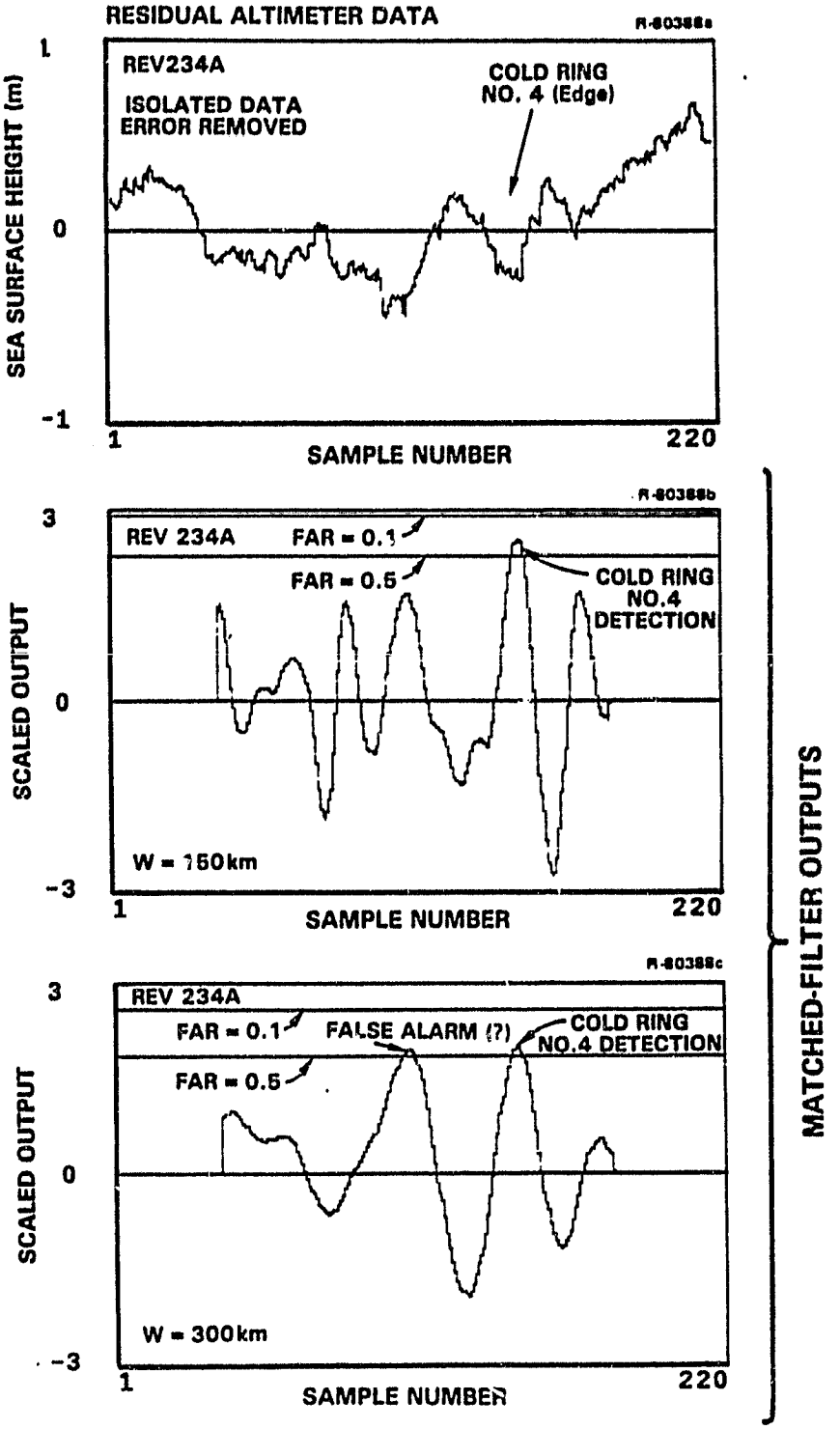

Figure 3.5-4 Demonstration of Cold-Ring Detection
SEASAT Rev. 234A

occurs at false-alarm rates in the range of 0.05 to 0.5 A/Mm

- The detection results are insensitive to localized data errors, which suggests that special preprocessing to correct erroneous data is unnecessary

- A two-pass technique for detecting boundary currents and ring currents is recommended for processing individual tracks of residual altimeter data: the first pass is used to detect possible boundary currents with a single model signature (one filter). If a boundary current is detected, the data set is truncated to remove the detected current signature. In the second pass, the truncated data set is processed with two or three filters, each matched to a different-width ring signature (e.g., 300, 200, 100 km). At each position along the track, the threshold detector uses the filter with the largest scaled output value.

- Since the model signatures for warm ring currents are the negatives of corresponding cold-ring signatures, a single filter serves to detect both cold and warm rings when a two-sided threshold detector is used. For example, if the filter is matched to a cold-ring signature and the detector uses a threshold TH > 0, then corresponding warm rings can be mapped by using a detector that flags those excursions of the filter output that fall below the negative threshold value -TH.

3.7 MATCHED-FILTER DETECTION THEORY

The theory of optimal matched filters for detecting deterministic signatures in additive colored noise is discussed in several text books (e.g., Refs. 15, 16, 18). The key results of that theory for ocean-current detection are summarized in the following.

Statement of the Detection Problem - The problem of detecting ocean-current signatures in residual altimeter data is formalized as follows.

GIVEN: $D(t)$ = time series of residual altimeter data

$m(t)$ = ocean-current signature time series

$N(t)$ = stationary Gaussian noise model for residual altimeter data that are free of current signature $m(t)$

T = specified time (location) in the data $D(t)$

A_s = unknown signature amplitude scale factor

H_T = hypothesis that $D(t) = N(t) + A_s m(t-T)$ with $A_s \neq 0$

H_0 = null hypothesis that $D(t) = N(t)$

FIND: An optimal decision rule for correctly choosing between hypotheses H_0 and H_T; and an optimal estimate of the amplitude A_s when H_T is chosen.

OPTIMALITY: Maximize the probability of correct detection for a specified probability of false alarm.

SOLUTION: Compute the likelihood ratio

$$LR = \frac{\text{Likelihood of } D(t) \text{ under } H_T}{\text{Likelihood of } D(t) \text{ under } H_0}$$

Select H_T when LR > threshold value.

Select H_0 when LR $\leq$ threshold value.

As depicted in Fig. 3.7-1, the optimal decision rule can be efficiently implemented by processing the residual altimeter data $D(t)$ with one matched filter and a threshold detector to test H_T against H_0 for all possible values of T. Once a detection is made (i.e., H_T is selected), the maximum-likelihood estimates of the location T and the amplitude scale factor A_s are easily computed from the matched-filter output.

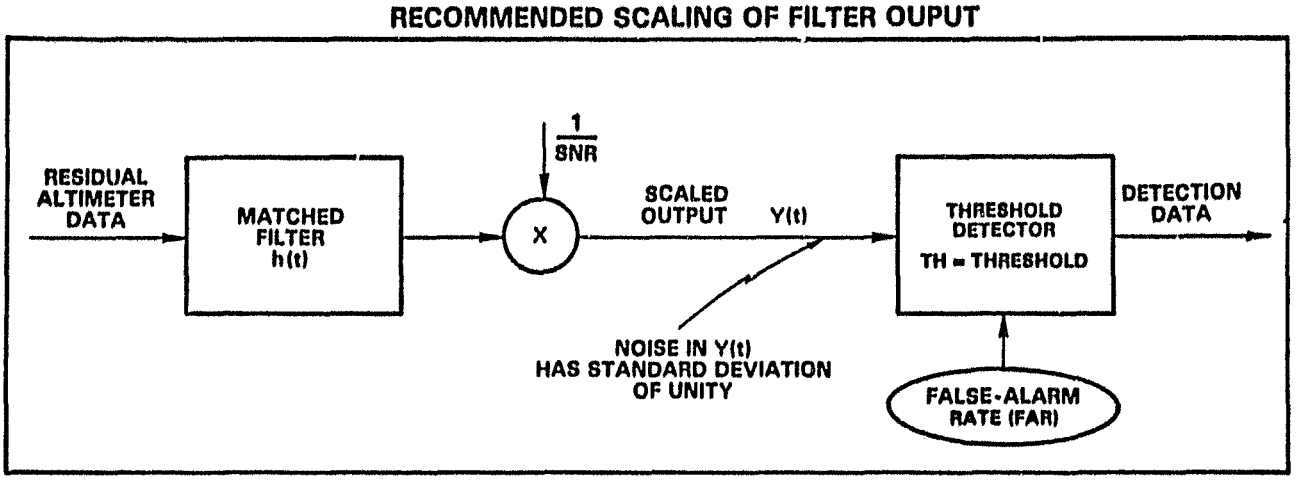

Figure 3.7-1 Matched-Filter Detector

Optimal Matched Filter - The optimal matched filter for long data sets is a convolution operator having the frequency response H(F) and the impulse response h(t) (e.g., Ref. 18, pp. 325-329)

$$h(t) = \int_{-\frac{1}{2}}^{\frac{1}{2}} H(F)\, e^{i2\pi Ft}\, dF \qquad (3.7\text{-}1)$$

$$H(F) = \frac{M(-F)}{S_{NN}(F)} \qquad (3.7\text{-}2)$$

F = normalized frequency (cycles/sample)

M(F) = Fourier transform of the ocean-current signature m(t)

$S_{NN}(F)$ = power spectrum of the residual altimetry N(t)

The Fourier transform of m(t) is defined as

$$M(F) = \sum_{t=-\infty}^{\infty} m(t)\, e^{-i2\pi Ft} \qquad (3.7\text{-}3)$$

$$m(t) = \int_{-\frac{1}{2}}^{\frac{1}{2}} M(F)\, e^{i2\pi Ft}\, dF \qquad (3.7\text{-}4)$$

The power spectrum of N(t) is the Fourier transform of the autocorrelation sequence $R_{NN}(t)$

$$R_{NN}(t) = E[N(t + t')\, N(t')] \qquad (3.7\text{-}5)$$

$$S_{NN}(F) = \sum_{t=-\infty}^{\infty} R_{NN}(t)\, e^{-i2\pi Ft} \qquad (3.7\text{-}6)$$

FIR Matched-Filter Algorithm - When the residual altimeter noise model N(t) is autoregressive (AR), the optimal matched filter can be implemented as a finite-impulse-response (FIR) filter. This means that the matched-filter impulse response h(t) has finite support, i.e., h(t) = 0 for $t < t_{min}$ and $t > t_{max}$, for finite t_{min} and t_{max}.

The AR model for the noise N(t) is a difference equation of order p driven by zero-mean Gaussian white noise W(t)

$$N(t) = C_1\, N(t\text{-}1) + C_2\, N(t\text{-}2) + \ldots + C_p\, N(t\text{-}p) + W(t) \qquad (3.7\text{-}7)$$

$$t = \ldots -1, 0, 1 \ldots$$

$$\text{Mean}(W(t)) = 0; \quad \text{Variance}(W(t)) = \sigma^2$$

The use of a Gaussian noise model is consistent with the observed Gaussian behavior of SEASAT-minus-geoid residual altimeter data described in Section 2.5.

From linear-system theory (Refs. 17 and 18), the power spectrum of N(t) is

$$S_{NN}(F) = \frac{\sigma^2}{G(F)\ G(-F)} \qquad (3.7\text{-}8)$$

$$G(F) = 1 - \sum_{k=1}^{p} C_k\ e^{-i2\pi Fk} \qquad (3.7\text{-}9)$$

From Eqs. 3.7-2 and 3.7-8, the matched filter frequency response may be expressed as

$$H(F) = \frac{M(-F)}{S_{NN}(F)} = \sigma^{-2} G(F)\ G(-F)\ M(-F) \qquad (3.7\text{-}10)$$

The Fourier transform of Eq. 3.7-10 yields the following expression for the impulse response h(t) of the matched filter (asterisks denote convolutions)

$$h(t) = \sigma^{-2} g(t) * g(-t) * m(-t) \qquad (3.7\text{-}11)$$

$$g(t) = \int_{-\frac{1}{2}}^{\frac{1}{2}} G(F)\ e^{i2\pi Ft}\ dF \qquad (3.7\text{-}12)$$

$$g(t) = 0;\ t < 0 \qquad (3.7\text{-}13)$$

$$g(0) = 1 \qquad (3.7\text{-}14)$$

$$g(1) = -C_1 \qquad (3.7\text{-}15)$$

$$\vdots$$

$$g(p) = -C_p \qquad (3.7\text{-}16)$$

$$g(t) = 0, \; t > p \qquad (3.7\text{-}17)$$

Since the convolutions in Eq. 3.7-11 contain only a finite number of non-zero terms when m(t) has finite support, the impulse response h(t) also has finite support. Figures 3.7-2 and 3.7-3 show examples of optimal impulse responses for cold-ring and Gulf-Stream signatures.

Matched-Filter Performance Measures - The theoretical rms signal-to-noise ratio of the matched filter is defined as

$$SNR = \frac{\text{Peak Filter Output Due to Signature } m(t)}{\text{Rms Filter Output Due to Noise } N(t)} \qquad (3.7\text{-}18)$$

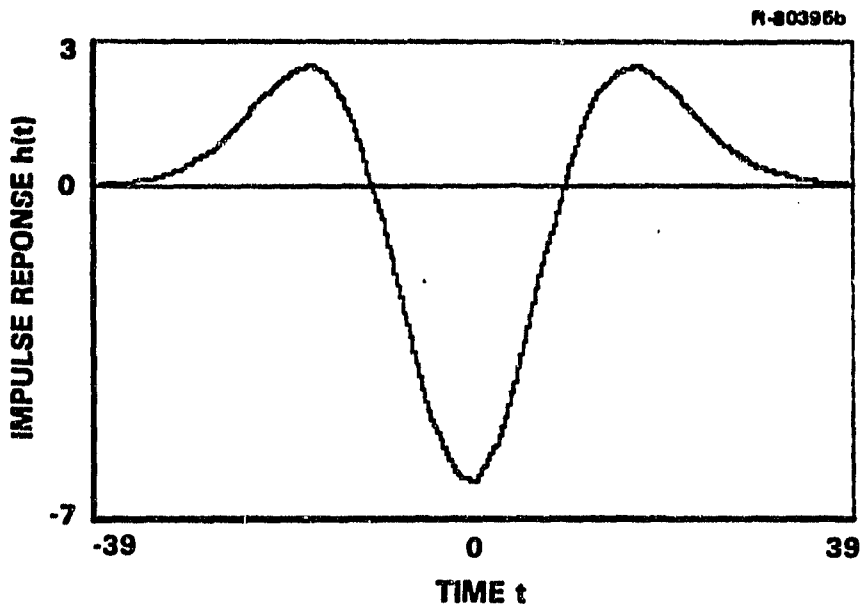

Figure 3.7-2 Typical Impulse Response of Filter for Detecting Cold Rings

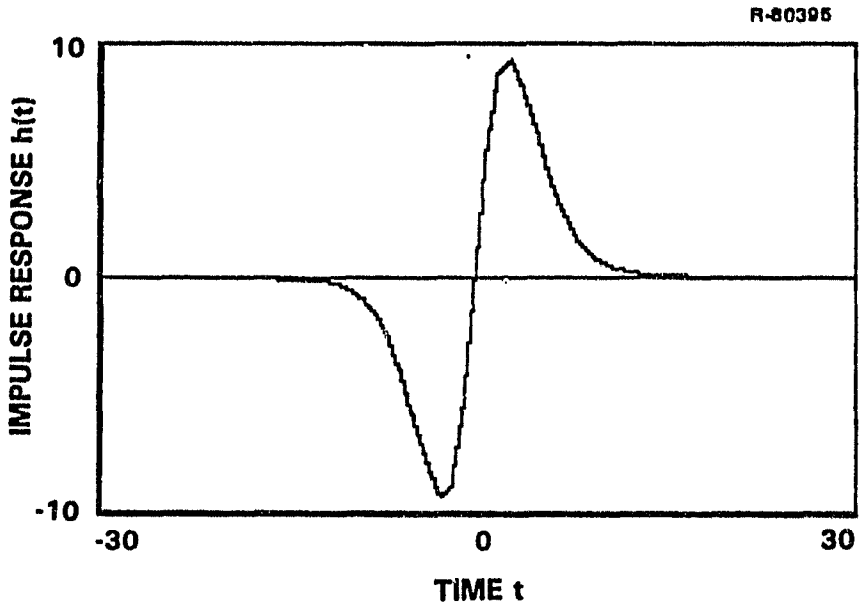

Figure 3.7-3 Typical Impulse Response for Gulf-Stream Detection

The SNR of an optimal matched filter is an important parameter. As shown in the Appendix, SNR may be computed with the formula

$$SNR = \sqrt{\sum_{j=-\infty}^{\infty} h(j)\, m(-j)} \qquad (3.7\text{-}19)$$

where only a finite number of terms contribute. The rms value of the noise in the filter output is numerically equal to SNR when the filter is optimized:

$$\text{Rms Noise in Filter Output} = SNR \qquad (3.7\text{-}20)$$

The peak filter output value due to the signature m(t) is also expressible in terms of SNR:

$$\text{Peak Filter Output Due to Signature } m(t) = SNR^2 \quad (3.7\text{-}21)$$

Equations 3.7-20 and 3.7-21 are derived in the Appendix.

Since the SNR equals the rms value of the modeled noise in the filtered output, it is convenient to scale the filter output by the factor 1/SNR as shown in Fig. 3.7-1. This yields a convenient test statistic Y(t) that contains a random component having a standard deviation of unity.

The mean output frequency F_m of the filter is a number that measures the average rate at which the filter output changes sign

$$F_m = \text{Half the Average Rate of Zero Crossings of Noise in Filter Output} \quad (3.7\text{-}22)$$

As shown in the Appendix, the mean output frequency of the Gaussian noise in the filter output is given by

$$F_m = \frac{1}{2\pi} \cos^{-1}[X/SNR^2] \text{ (cycles/sample)} \quad (3.7\text{-}23)$$

where

$$X = \sum_{k=-\infty}^{\infty} h(k)\, m(1-k) \quad (3.7\text{-}24)$$

3.8 THRESHOLD DETECTION THEORY

As depicted in Fig. 3.7-1, the threshold detector compares the sequence of scaled test statistics Y(t) from the matched filter against a detection threshold. When Y(t) exceeds the threshold, an alarm is said to occur. These alarms are classified into three categories:

- Correct Detection caused by occurrences of modeled current signatures in the residual altimeter data
- False Alarms caused by random excursions of the modeled noise in the residual altimeter data
- Unmodeled Detections caused by unmodeled current signatures or unmodeled noise in the residual altimeter data.

The statistics of correct detections and false alarms are computed for the specific ocean-current signature and the specific noise model for which the filter was designed. On the basis of these statistics, the expected average performance of the detector is predicted, and the detection threshold is adjusted for a desired tradeoff between detection probabilities and false-alarm rates.

Formulas are listed below for computing the following performance statistics of the detector: the probability of false alarms; the average false-alarm rate, the maximum-likelihood estimates of signature location and amplitude (and their rms accuracies), and the probability of detecting a signature with a prescribed amplitude.

Probability of False Alarm - Let TH denote the detection threshold and P_f the probability of a false alarm. The

P_f is the probability that the noise component alone in Y(t) will exceed TH and is given by the standardized normal probability distribution function:

$$P_f = \text{Prob}\{Y(t) > TH; \text{ noise alone}\} \tag{3.8-1}$$

$$P_f = Q(TH) = \int_{TH}^{\infty} \frac{1}{\sqrt{2\pi}} \exp(-x^2/2)\, dx \tag{3.8-2}$$

The detection threshold that yields a prescribed probability of false alarm is

$$TH = Q^{-1}(P_f) \tag{3.8-3}$$

Average False-Alarm Rate - The threshold detector processes data from individual tracks of altimeter data; it is often reasonable to set the detection threshold so that a specified number of false alarms is expected to occur per unit distance along the track (expressed in the units of alarms per data sample). This false-alarm rate (FAR) is computed as

$$FAR = F_m \exp(-TH^2/2) \text{ (alarms/sample)} \tag{3.8-4}$$

F_m = mean output frequency of modeled noise in filter output

Equation 3.8-4 is derived from results in Ref. 17, p. 492. The expected number of false alarms (EN) along a track of data having N samples of the test statistic Y(t) is

$$EN = N \cdot FAR \tag{3.8-5}$$

Detection Threshold - It is recommended that the detection threshold TH be chosen to yield a specified false-alarm rate FAR in accordance with the equation

$$TH = \sqrt{-2\ \ln(FAR/F_m)} \qquad (3.8\text{-}6)$$

Equation 3.8-6 is obtained by solving Eq. 3.8-4 for TH.

Detected Signature Location and Amplitude - The maximum-likelihood estimate of the location of a detected signature is the value of t for which Y(t) achieves its local maximum value above the threshold TH. Let t_o denote this estimate of signature location. The Cramer-Rao (C-R) lower bound on the rms error of this estimate depends on the maximum scaled filter output $Y(t_o)$:

$$\text{C-R Lower Bound} = \frac{1}{2\pi\ F_m\ Y(t_o)}\ \text{(samples)} \qquad (3.8\text{-}7)$$

This lower bound on the variance of t_o can be re-expressed in units of kilometers

$$\text{C-R Lower Bound} = \frac{v\ \ 10^{-3}}{2\pi\ F_m\ f_s\ Y(t_o)}\ \text{(km)} \qquad (3.8\text{-}8)$$

v = Altimeter along-track velocity (m/s)

f_s = Data sampling frequency (samples/sec)

Nominal values for SEASAT altimeter data are v = 6700 m/s and f_s = 1.0 sample/sec. The false-alarm rate can also be expressed in terms of distance:

$$\text{FAR (alarms/sample)} = \frac{v\ 10^{-6}}{f_s}\ \text{[FAR (alarms/megameter)]} \qquad (3.8\text{-}9)$$

The maximum-likelihood estimate of the signature amplitude scale factor A_s is

$$\hat{A}_s = \frac{Y(t_o)}{SNR} \qquad (3.8\text{-}10)$$

and the rms (one-sigma) error in this estimate is 1/SNR. The maximum-likelihood estimate of the detected signature is then $\hat{A}_s \cdot m(t-t_o)$.

Probability of Detection - The probability of detecting the model signature $m(t-t_o)$ with a filter matched to $m(t)$ and a detector operating with threshold TH is

$$P_d = \text{Prob}\ \{Y(t_o) > TH;\ m(t) + \text{noise}\} \qquad (3.8\text{-}11)$$

The peak filter output due to $m(t-t_o)$ is SNR^2 (Eq. 3.7-21). Therefore the peak scaled output is

$$Y(t_o) = SNR + (\text{zero-mean unit-variance noise}) \qquad (3.8\text{-}12)$$

Equation 3.8-12 implies that Eq. 3.8-11 may be expressed in the equivalent form

$$P_d = \text{Prob} = \{\ \text{noise} > TH - SNR\} \qquad (3.8\text{-}13)$$

$$P_d = Q(TH - SNR) \qquad (3.8\text{-}14)$$

For studying the ability of a matched filter to discriminate between different signatures, it is useful to compute the probability of detecting a signature $m'(t-t_o)$ when the filter is matched to a different signature $m(t)$. Let SNR be the rms signal-to-noise ratio of the filter with respect to $m(t)$ (Eq. 3.7-19). Let the peak output of the filter due to the other signature $m'(t-t_o)$ be denoted x'. If this peak output occurs at time t_o', then

$$x' = \sum_{k=-\infty}^{\infty} h(k)\, m'(t_o' - k) \qquad (3.8\text{-}15)$$

The rms value of the noise in the filter output is SNR (Eq. 3.7-20). Therefore, the rms signal-to-noise ratio (SNR') of the filter with respect to signature $m'(t-t_o)$ is

$$SNR' = x'/SNR \qquad (3.8\text{-}16)$$

The probability of detecting signature m'(t) with a detection threshold TH as in Fig. 3.7-1 is therefore

$$P_d(m') = Q(TH - SNR') \qquad (3.8\text{-}17)$$

In the special case where $m'(t) = A_s\, m(t)$, the probability of correct detection is

$$P_d(A_s\, m) = Q(TH - A_s \cdot SNR) \qquad (3.8\text{-}18)$$

3.9 SAMPLE PARAMETER VALUES

Gulf-Stream Detection - Table 3.9-1 shows typical parameter values computed by the detection algorithm operating on residual SEASAT altimeter data from Rev. 234A. The table permits a comparison of parameter values for two Gulf-Stream model signatures that differ only in their heights. Since their widths are the same (100 km), both of these signatures can be optimally detected by a single matched filter.

TABLE 3.9-1
SAMPLE PARAMETER VALUES FOR GULF-STREAM DETECTION

SEASAT REV 234A						
MATCHED-FILTER PARAMETERS			THRESHOLD-DETECTOR PARAMETERS			
MODEL SIGNATURE	SNR	F_m (cyc/Mm)	C-R LOCATION ERROR BOUND (km)	FAR (A/Mm)	TH	P_d
HEIGHT = 1.4 m WIDTH = 100 km	7.2	4.1	5	10^{-6}	5.5	0.96
				10^{-4}	4.6	1.00
				10^{-2}	3.5	1.00
HEIGHT = 1.0 m WIDTH = 100 km	5.2	4.1	7	10^{-6}	5.5	0.36
				10^{-4}	4.6	0.71
				10^{-2}	3.5	0.95

The larger 1.4-m signature yields an rms signal-to-noise ratio (SNR) of 7.2 while for the smaller 1.0-m signature SNR = 5.2. The mean frequency (F_m) of the noise in the filter outputs is 4.1 cycles/megameter for both filters, because F_m is independent of the model signature amplitude. The Cramer-Rao (C-R) rms error bounds on locating the two signatures are 5 km and 7 km; the smaller error corresponds to the larger-amplitude signature.

The right side of Table 3.9-1 displays parameter values for the threshold detector that compares the scaled output Y(t) of the matched filters with the threshold TH. Three false-alarm rates (FAR) are considered, ranging from 10^{-2} alarm/megameter (A/Mm) to 10^{-6} A/Mm. The detection thresholds (TH) range from 3.5 to 5.5 independently of the model signature

amplitude. The interpretation of the threshold values is simple because the test statistic Y(t) is scaled to have a variance of unity. For example, with a threshold of 3.5, a false alarm occurs if the noise in Y(t) makes a positive excursion that exceeds 3.5 standard deviations from the mean (zero). The last column in the table lists the probabilities of detecting the signatures with the three false-alarm rates. The results show that the probability of detecting the smaller signature is sensitive to the false-alarm rate. The results in this table verify that typical Gulf-Stream signatures are expected to be reliably detected.

Cold-Ring Detection - Table 4.9-2 shows sample parameter values computed by the detection algorithm operating on residual SEASAT altimeter data for Rev. 234A. This table compares parameter values for two cold-ring model signatures that differ in both width and amplitude. Because their widths are different, two different matched filters are required to detect these signatures optimally.

The filter for the narrower (150-km) signature has the larger mean frequency (F_m) and the lower Cramer-Rao location error bound. This occurs because the 150-km signature is more compact and leads to a higher signal-to-noise ratio than the 300-km signature. The 300-km signature is slightly more difficult to distinguish from the noise in the altimeter data as revealed by the values of SNR and the probabilities of detection (P_d).

A study of the parameter values for the threshold detector shows that the cold-ring signatures are detectable ($P_d > 0.8$) at false-alarm rates of FAR > 0.1 alarm/megameter (FAR > 1 alarm per 10,000 km of data).

TABLE 3.9-2
SAMPLE PARAMETER VALUES FOR COLD-RING DETECTION

SEASAT REV 234A						
MATCHED-FILTER PARAMETERS			THRESHOLD-DETECTOR PARAMETERS			
MODEL SIGNATURE	SNR	F_m (cyc/Mm)	C-R LOCATION ERROR BOUND (km)	FAR (A/Mm)	TH	P_d
DEPTH = 0.5 m				0.01	3.6	0.61
WIDTH = 150 km	3.9	6.7	6	0.1	2.9	0.84
				0.5	2.3	0.95
DEPTH = 0.7 m				0.01	3.4	0.49
WIDTH = 300 km	3.4	3.0	16	0.1	2.6	0.77
				0.5	1.9	0.93

3.10 ALGORITHM CAPABILITY FOR DISCRIMINATING BETWEEN TWO COLD RINGS

Matched filters can be used to discriminate between cold-ring signatures having different widths. To study this discrimination capability, the probability of detection is plotted as a function of the false-alarm rate for signatures of different sizes. These plots are like the "operating characteristic" of the detector, except that the false-alarm rate is used in place of the false-alarm probability.

As an example, consider a filter that is matched to a 0.5-m × 150-km cold-ring signature (the signature is given by Eq. 3.3-1 with D = 0.5 m and W = 150 km). For a typical track of residual SEASAT altimeter data in the western North Atlantic, the filter has an rms signal-to-noise ratio (SNR, Eq. 3.7-19)

of 3.9. The probability of detection (P_d, Eq. 3.8-14) for this SNR is plotted as function of the false-alarm rate (FAR, Eq. 3.8-4) in the upper part of Fig. 3.10-1. The different values of FAR correspond to different detection thresholds.

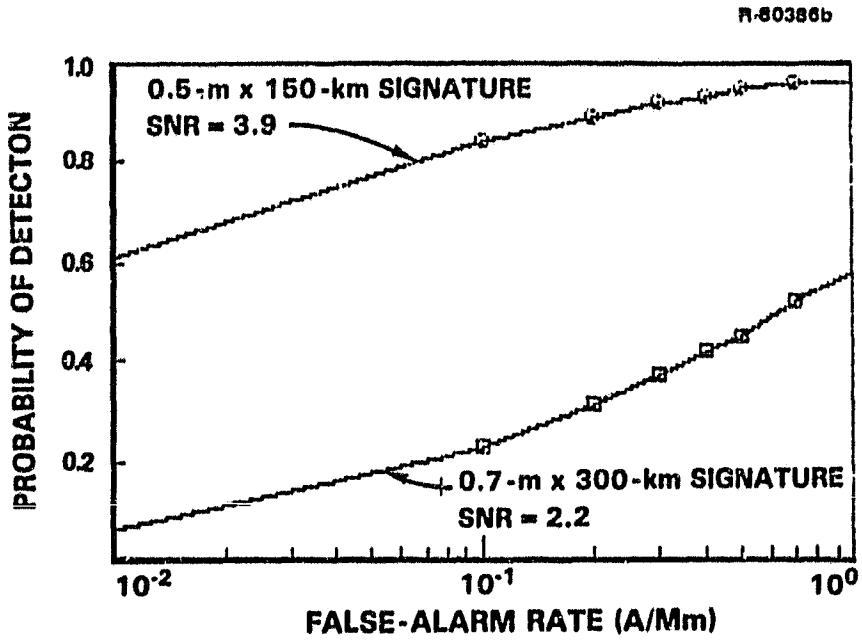

Figure 3.10-1 Filter Matched to 0.5-m × 150-km Signature

When the 150-km filter is used to detect (suboptimally) a larger 0.7-m × 300-km cold-ring signature, the probabilities of detection are significantly reduced as indicated by the curve in the lower part of Fig. 3.10-1. (The SNR with the 300-km signature is 2.2 as computed with Eq. 3.8-16, and the P_d is computed with Eq. 3.8-17.) The vertical separation of the curves in Fig. 3.10-1 is a quantitative measure of the discrimination capability of the 150-km filter as a function of FAR.

Figure 3.10-2 is like Fig. 3.10-1, except the matched filter is optimized here to detect the wider 300-km signature.

Because the filter is optimized for the wider signature, the SNR (3.4) is larger than it is in Fig. 3.10-1, where SNR = 2.2. The performance of the 300-km filter for detecting (suboptimally) the 150-km signature is depicted by the curve in the lower part of Fig. 3.10-2. A comparison of Figs. 3.10-1 and 3.10-2 shows that the wider 300-km filter is less discriminating and more robust than the narrower 150-km filter, as quantified by the smaller separation of the curves in Fig. 3.10-2.

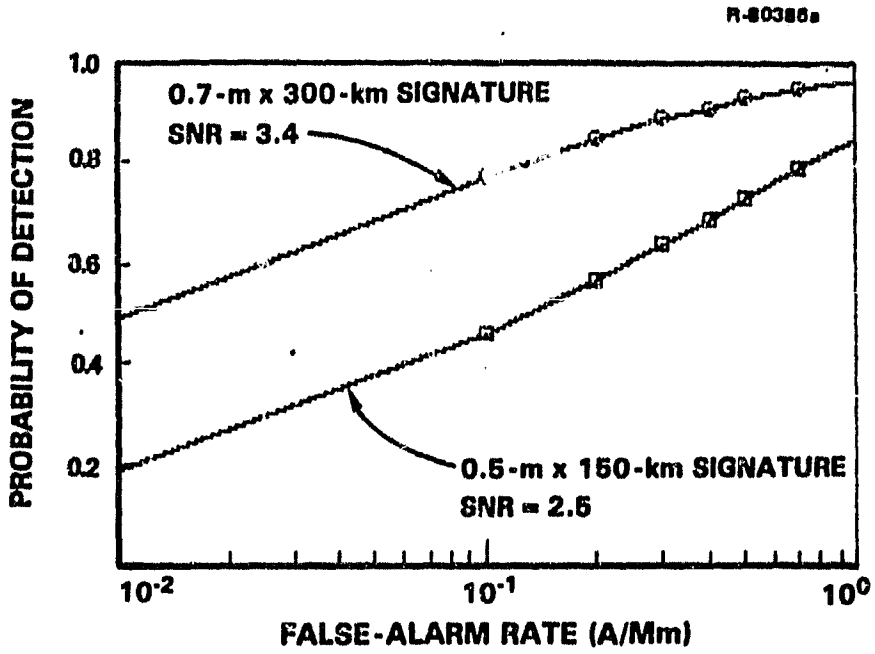

Figure 3.10-2 Filter Matched to 0.7-m × 300-km Signature

The results presented here for detecting cold rings are considered typical and may be summarized as follows:

- The filter matched to the narrower signature is the more discriminating
- The filter matched to the wider signature is the more robust.

3.11 SUMMARY OF OCEAN-CURRENT DETECTION STUDY

An ocean-current detection algorithm for processing single tracks of residual satellite altimeter data has been developed and verified. The algorithm is data-adaptive and is based on autoregressive statistical modeling, matched detection filters, and models for generic altimetric signatures caused by boundary and ring currents.

The algorithm performance was verified for Gulf-Stream and cold-ring detections using SEASAT altimeter data, the Marsh-Chang geoid, and surface truth data in the western North Atlantic. The algorithm performance was quantified in terms of

- False-Alarm Rates
- Probabilities of Detection
- Location Estimation Errors
- Signal-to-Noise Ratios
- Mean Output Frequencies.

The study results indicate that the automatic detection of Gulf-Stream and cold-ring signatures is feasible with a processing time (IBM Model 4341 computer) of approximately 0.5 sec per data track using one matched filter. The algorithm is also applicable to warm-ring detection.

The results of verifying the algorithm with SEASAT data lead to the following conclusions:

- The algorithm performance is insensitive to localized data errors
- Filters matched to narrower signatures discriminate against wider signatures

- Filters matched to wider signatures are robust; i.e., they are especially insensitive to localized data errors, and they are able to detect (suboptimally) narrower signatures of similar shape.

Formal specifications for the detection algorithm are given in Ref. 19.

3.12 AREAS FOR FUTURE STUDY IN OCEAN-CURRENT DETECTION

The following three areas are suggested for future study.

- Quantify the sensitivity of the algorithm performance to geoid estimation error. Although the algorithm is data adaptive and can therefore be used with any geoid estimates, the sensitivity of the algorithm performance to the accuracy of the geoid estimates remains to be studied.

- Develop a recursive implementation for the matched filters. Because the altimeter data are modeled autoregressively, the matched filters can be rigorously implemented with a recursive algorithm, as opposed to the straight convolutions used in the present algorithm. A recursive implementation will reduce the time to filter the data by a factor of five and will be useful for applications to multi-signature detectors for ring currents.

- Process all relevant SEASAT data in the western North Atlantic. This will provide additional statistics describing the algorithm performance in an operational setting. The western North Atlantic has the distinction of being an oceanographically interesting region for which geoid estimates and surface truth data are available.

4. GEOSTROPHIC-VELOCITY ESTIMATION ALGORITHM

4.1 INTRODUCTION

A nearly geostrophic boundary current, such as the Gulf Stream in the western North Atlantic, produces a characteristic signature in satellite altimeter data where the satellite subtrack intersects the current. The along-track slope of this signature is proportional to the cross-track component of the geostrophic current velocity as expressed by the geostrophic relation. Therefore, the cross-track geostrophic velocity can be inferred from estimates of the signature slope. This chapter describes a velocity estimation algorithm based on estimating signature slopes via matched filtering.

The chapter is organized as follows. Section 4.2 describes an automated data-adaptive algorithm for computing estimates of geostrophic velocity. The algorithm uses the matched-filtering detection algorithm described in Chapter 3. Verifications of the velocity estimation algorithm with SEASAT altimeter data are discussed in Section 4.3. A summary and conclusions are presented in Section 4.4, and suggestions for further study are offered in Section 4.5.

4.2 ALGORITHM DESCRIPTION

The velocity estimation algorithm processes single tracks of residual satellite altimeter data (sea surface height minus geoid estimates). Each track of data is assumed to have been previously processed with a single matched filter that detected a boundary-current signature in the data.

The outputs of the algorithm are the estimated along-track location of the maximum geostrophic velocity, the estimated maximum cross-track geostrophic velocity, and rms accuracy measures for the location and velocity estimates.

The algorithm uses several matched filters to estimate the parameters W_s and A_s in the following hyperbolic-tangent model signature (which is discussed in Section 3.3):

$$H(x) = - A_s \, (A/2) \tanh(3 \, x/W_s) \qquad (4.2\text{-}1)$$

$H(x)$ = Sea surface height

x = Position along subtrack

A = Amplitude of model signature (arbitrary initial value used to design matched filter)

A_s = Amplitude scale factor (chosen for best fit with data)

W_s = Signature width (90 percent height change).

The cross-track geostrophic velocity is estimated from the geostrophic relation applied to the slope of the model signature. By using equations in Section 3.3, the cross-track velocity implied by the model signature can be written as

$$V_c(x) = A_s \frac{3 \, g \, A}{2 \, f \, W_s} \operatorname{sech}^2(3 \, x/W_s) \qquad (4.2\text{-}2)$$

$V_c(x)$ = Cross-track component of geostrophic velocity

x = Position along subtrack

$f = 2\Omega\sin\phi$ = Coriolis parameter

Ω = Earth's rotational velocity

ϕ = North latitude

g = Acceleration of gravity.

The maximum cross-track geostrophic velocity is

$$\left[V_c\right]_{max} = V_c(0) = A_s \frac{3\ g\ A}{2\ f\ W_s} \qquad (4.2\text{-}3)$$

The uncertainty in the velocity estimate is estimated from the rms uncertainty in the estimate of parameter A_s. As discussed in the following, the algorithm consists of five steps.

Step 1 - The residual altimeter data are processed with five matched filters, each optimized for detecting a different-width signature. For example, signature widths of 50, 60, 75, 100 and 150 km are reasonable for the Gulf Stream in the western North Atlantic.

Step 2 - The most likely width of the signature in the altimeter data is estimated by comparing the scaled outputs (Y(t) in Fig. 3.7-1)) from each of the matched filters to determine that filter which yields the largest response to the signature. This filter is said to be best-matched to the signature in the data. The signature width of this filter is selected as the best estimate $\hat{W}_s$ for the width of the signature in the data.

Step 3 - The maximum-likelihood estimate $\hat{A}_s$ of the amplitude scale factor is computed from the observed maximum output $Y(t_o)$ of the best-matched filter in accordance with the theory discussed in Section 3.8:

$$\hat{A}_s = Y(t_o)/SNR \qquad (4.2\text{-}4)$$

SNR = Theoretical rms signal-to-noise ratio of the best-matched filter

SNR is computed by using Eq. 3.7-19. Since $Y(t_o)$ is modeled as a sample from a random process with unit variance, the rms uncertainty $\delta\hat{A}_s$ in the estimate $\hat{A}_s$ is given as

$$\delta\hat{A}_s = 1/SNR = \text{Standard deviation of } \hat{A}_s \qquad (4.2\text{-}5)$$

The estimated maximum cross-track geostrophic velocity $\hat{V}_c(0)$ and its rms uncertainty $\delta\hat{V}_c(0)$ are given as

$$\hat{V}_c(0) = \hat{A}_s \frac{3\ g\ A}{2\ f\ \hat{W}_s} \qquad (4.2\text{-}6)$$

$$\delta\hat{V}_c(0) = \delta\hat{A}_s \frac{3\ g\ A}{2\ f\ \hat{W}_s} \qquad (4.2\text{-}7)$$

Equation 4.2-7 is a useful working estimate of velocity estimation accuracy. It is recognized that a more complicated error analysis is possible, which accounts for the error $\delta\hat{W}_s$ in $\hat{W}_s$ and the correlation between $\delta\hat{W}_s$ and $\delta\hat{A}_s$. Since no stochastic model is available to support such an analysis, the simpler estimate in Eq. 4.2-7 is recommended.

Step 4 - The maximum-likelihood estimate of the location of the maximum geostrophic velocity is that time t_o at which the best-matched filter achieves its maximum scaled output $Y(t_o)$. The rms uncertainty δt_o of this estimate is given by the Cramer-Rao lower bound (Eq. 3.8-7):

$$\delta t_o = \frac{1}{2\pi\ F_m\ Y(t_o)} \qquad (4.2\text{-}8)$$

where the mean frequency F_m is computed by using Eq. 3.7-23.

4.3 DEMONSTRATION OF GULF-STREAM VELOCITY ESTIMATION

The performance of the velocity estimation algorithm is verified by using it to estimate Gulf-Stream velocities. Four examples are presented, which use the same tracks of SEASAT residual altimeter data as the demonstrations of the detection algorithm in Sections 3.4 and 3.5. The time required to process a track of data containing one boundary-current signature is 1.5 seconds on an IBM Model 4341 computer. (Only the data in the vicinity of the detected boundary current are used for geostrophic velocity estimation.)

Example 1 - Figure 4.3-1 shows two plots of sea surface height as a function of position along the SEASAT subtrack for Rev. 234A. The solid curve is the residual altimeter data that were used as input to the velocity estimation algorithm described in Section 4.2. The dashed curve is the tanh model signature that the algorithm fitted to these data. The vertical positioning of the model signature has no effect on the estimate of geostrophic velocity, which depends only on the slope of the signature. Therefore, the algorithm does not estimate the vertical positioning of the signature; the vertical position of the tanh signature is manually selected in these examples to provide easy visual comparisons with the SEASAT data. In contrast, the vertical and horizontal scales and the horizontal position of the tanh signature are each important for estimating the current velocity; these features of the signature are determined automatically by the algorithm. The fit of the tanh signature to the SEASAT data looks reasonable in the Gulf-Stream transition region centered on data sample number 233. The maximum cross-track component of the geostrophic velocity is 1.54 m/s (Eq. 4.2-6) with an estimated rms accuracy (Eq. 4.2-7) of 0.22 m/s (14 percent of the velocity estimate).

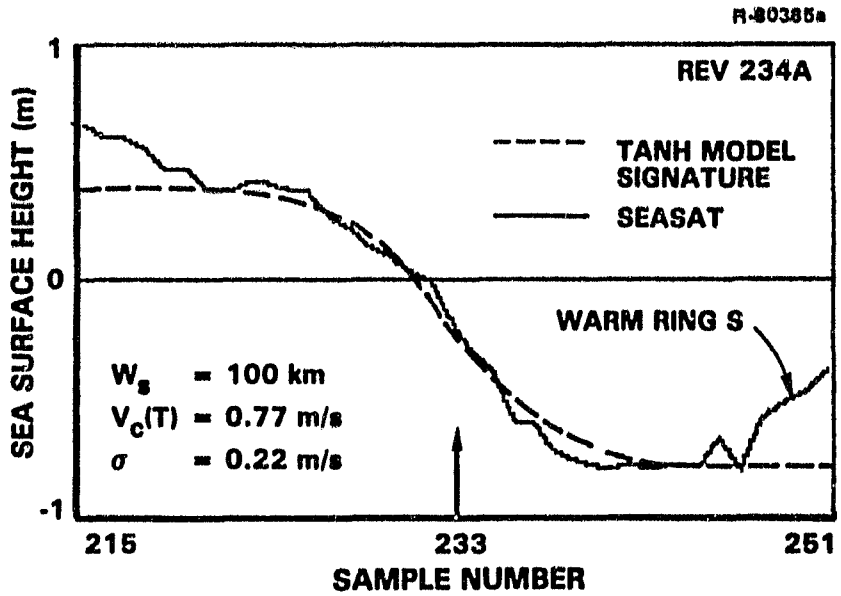

Figure 4.3-1 Gulf-Stream Signatures, Rev. 234A

Example 2 - Figure 4.3-2 shows data for SEASAT Rev. 277A. The estimation algorithm provides a reasonable fit to the altimeter data in the transition region centered on sample number 233, where the algorithm estimates that the cross-track velocity achieves a maximum value of 2.82 m/s. The rms accuracy is estimated by the algorithm to be 0.70 m/s (25 percent of the velocity estimate). This estimate of rms uncertainty may be too large, because in this example the algorithm used data (for noise modeling) that contained significant data errors due to the island of Bermuda as depicted in Figure. 3.4-4.

The deviation between the tanh signature and the altimeter data on the right of Fig. 4.3-2 is caused by warm ring U, whose existence is verified by independent oceanographic data (Ref. 6). Fortunately, the estimation of maximum geostrophic velocities requires only that the sea surface slope be estimated in the relatively narrow transition zone where the geostrophic flow is located.

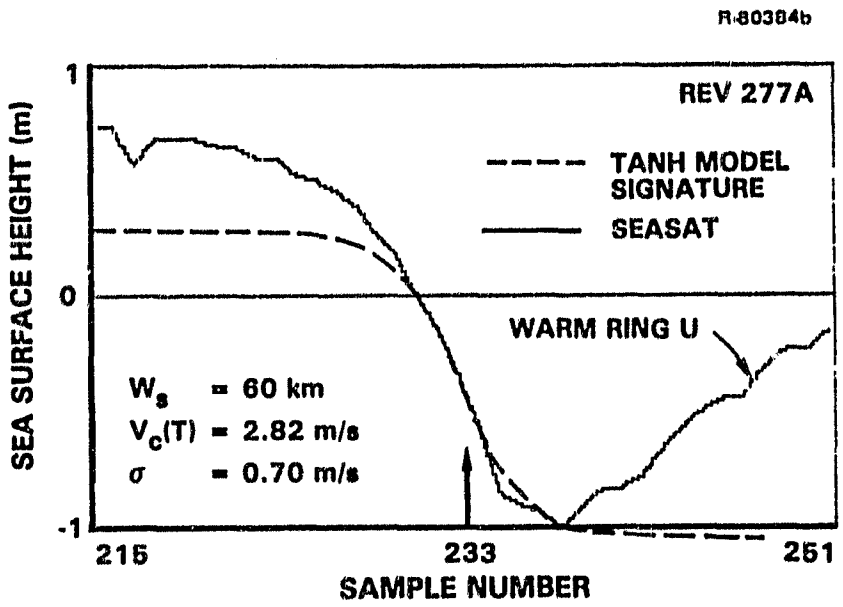

Figure 4.3-2 Gulf-Stream Signatures, Rev. 277A

Examples 3 and 4 - The model signatures selected by the estimation algorithm for SEASAT Revs. 478A and 572D are shown in Figs. 4.3-3 and 4.3-4. The tanh signatures provide reasonable fits with the altimeter data in the transition regions of the Gulf Stream. The results in Fig. 4.3-4 demonstrate that the fit of the model signatures to the maximum-slope of the altimeter data is insensitive to nearby ring currents. The estimated maximum cross-track geostrophic velocity for Rev. 478A is 1.78 m/s with an estimated rms accuracy of 0.36 m/s (20 percent of the velocity estimate). For Rev. 572D the estimated maximum velocity is 1.96 m/s with an estimted rms accuracy of 0.26 m/s (13 percent of the velocity estimate).

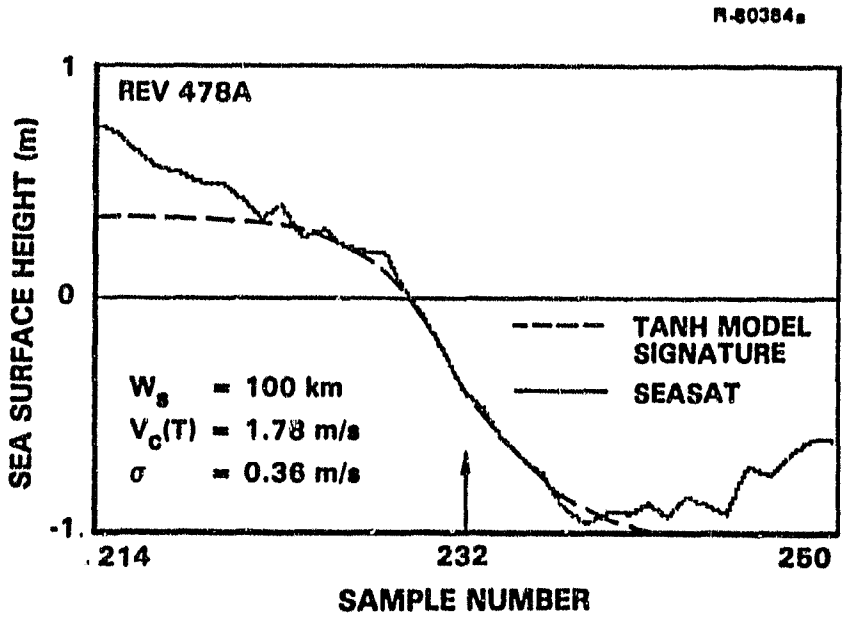

Figure 4.3-3 Gulf-Stream Signatures, Rev. 478A

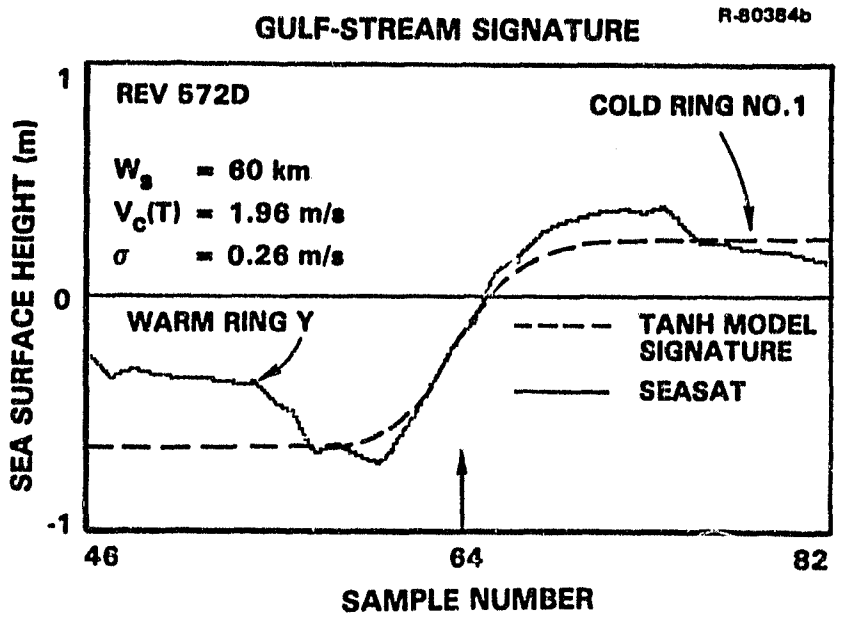

Figure 4.3-4 Gulf-Stream Signatures, Rev. 572D

4.4 SUMMARY AND CONCLUSIONS OF GEOSTROPHIC-VELOCITY ESTIMATION STUDY

Summary - An algorithm has been developed to estimate the velocities of geostrophic surface currents by the analysis of single tracks of satellite altimeter data. The algorithm performance is verified by four examples of Gulf-Stream velocity estimation using SEASAT altimeter data and the Marsh-Chang geoid.

The algorithm utilizes the data-adaptive matched-filter algorithm developed for ocean-current detection and automatically performs the following analysis of the altimeter data. A bank of five matched filters estimates the location and the best width and amplitude for a model signature of the sea-surface height where the satellite subtrack crosses the geostrophic current. The cross-track component of the geostrophic current velocity is estimated from the slope of the model signature by using the geostrophic relation. The rms accuracy of the velocity estimate is computed from the theoretical rms uncertainty of a maximum-likelihood estimate of the signature amplitude.

Conclusions - The results of this study lead to the following conclusions:

- The automated estimation of cross-track geostrophic velocities from satellite altimeter data is feasible for boundary currents such as the Gulf Stream
- The velocity estimation algorithm is a simple extension of the data-adaptive matched-filter algorithm for detecting and locating boundary and ring currents
- Processing time is about 1.5 sec per data track using an IBM Model 4341 computer; 0.5 sec for detecting the current signature with one matched filter, and

1 sec for estimating the geostrophic current velocity with four additional filters operating on the data in the vicinity of the current signature

- The performance of the velocity estimation algorithm is insensitive to isolated data errors and to the occurrence of warm-ring and cold-ring signatures in the altimeter data.

Formal specifications for the velocity estimation algorithm are given in Ref. 19.

4.5 SUBJECTS FOR FURTHER STUDY

Based on the results of this investigation, the following subjects are recommended for further study.

- Determine the best choice of model signatures. The use of five model signatures in this study (50, 60, 75, 100, and 150 km) yields reasonable results, but other choices may be preferable in terms of the trade-offs between accuracy and computational complexity.

- Quantify the sensitivity of the velocity estimates to the accuracy of the geoid estimates. Although the algorithm is data-adaptive and can be used with any geoid estimates, the sensitivity of the velocity estimates to geoid error has not been studied.

- Compare current velocities estimated by the algorithm with surface truth data. Because no surface truth data on Gulf-Stream velocities were available for the subtracks used in this study, a direct comparison of satellite-derived velocities with surface data has not been possible.

- Develop a faster recursive algorithm for implementing the matched filters in the algorithm. Such recursive algorithms are feasible, because the altimeter data noise model is autoregressive. A recursive algorithm would permit larger numbers of model signatures to be used for increased accuracy. Alternatively, recursive filters could be used to reduce the computational requirements.

5. SUMMARY, CONCLUSIONS, AND RECOMMENDATIONS

5.1 SUMMARY

This report documents the study of the oceanographic information content of SEASAT altimeter data and describes the development of NOSS algorithms for ocean-current mapping and their verification with SEASAT altimeter data. The inputs to the algorithms are individual tracks of residual satellite radar altimeter data from which estimated geoid profiles have been subtracted. The algorithms are based on the fact that cold-core and warm-core current rings and boundary currents can be detected by identifying the occurrence of characteristic sea-surface height signatures in the residual altimeter data. In the case of nearly geostrophic boundary currents, the cross-track component of the current velocity can be inferred by estimating the along-track sea-surface slope from the altimeter data and then using the geostrophic equation to compute the velocity.

In the study of the oceanographic information content of SEASAT altimeter data, autoregressive modeling techniques were used to analyze the statistical behavior of residual altimeter data. The analysis results show that residual altimeter data have the statistical properties of Gaussian random noise with a correlation structure that varies from track to track. The results of the study were used as a basis for the development of the NOSS algorithms.

The NOSS algorithms are based on optimal matched filters, which are used to detect, locate, and estimate the amplitudes of generic current signatures in the residual altimeter

data. The algorithms automatically analyze each track of residual altimeter data and compute an optimal autoregressive model for the noise signal in the data. Using this noise model, together with a parametric model for the deterministic ocean-current signature that is to be detected, the algorithm designs a statistically optimal matched-filter detector for discriminating between the noise and the signature. The detector is optimal in the sense that the probability of detecting the ocean-current signature is maximized for a specified probability of false alarm (a false alarm occurs when the random noise excursions in the altimeter data masquerade as a current signature and cause a false detection). The algorithm adjusts the sensitivity of the detector to achieve a specified average false-alarm rate (e.g., 1 false alarm per 10,000 km of data along the satellite subtrack). The algorithm performance was demonstrated with SEASAT altimeter data and Marsh-Chang geoid estimates in the western North Atlantic, where known boundary-current and ring-current signatures occur in the altimeter data.

The algorithm for estimating the geostrophic velocities of boundary currents employs a bank of five matched-filter detectors; each filter is matched to a different width for the current signature. The algorithm determines that signature width which is most probable (given the available altimeter data) and computes a maximum-likelihood estimate of the current signature amplitude. From this information, the algorithm estimates the maximum along-track slope of the sea surface and uses the geostrophic equation to compute the estimated cross-track component of geostrophic velocity. The rms accuracy of the velocity estimate is also computed by using the Cramer-Rao lower bound on the variance of the estimated signature amplitude. The algorithm performance was demonstrated with SEASAT data containing Gulf-Stream signatures.

The formal specifications for the NOSS algorithms are documented in Ref. 19.

5.2 CONCLUSIONS

The primary conclusions of this study are summarized in the following. More detailed discussions are provided in Section 2.8, 3.6, 3.11, and 4.4.

- The residual SEASAT altimeter data (SSH minus geoid) analyzed in this study has statistical properties of correlated Gaussian random noise. No systematic departure from Gaussian behavior was observed.

- By using a unique Kalman smoother to process each track of data, the time-varying mesoscale SSH waveforms in sets of difference data from nearly repeating SEASAT tracks can be estimated with an average theoretical rms accuracy of 2 cm. The results of using such smoothers on data from the region south of Iceland indicate that statistically significant mesoscale variations (larger than 6 cm) occur during several of the 3-day intervals between Revs.

- Verification tests with residual SEASAT altimeter data from the western North Atlantic indicate that the Gulf Stream is reliably detected and located with the NOSS detection algorithm developed in this study. The required computing time is less than 0.5 sec per track using an IBM 4341 computer.

- The feasibility of using the NOSS detection algorithm to detect and locate cold-core current rings in the western North Atlantic was verified with residual SEASAT altimeter data. To increase the probability of detection and to discriminate between rings of different widths, it is

recommended that each track of data be processed by the algorithm with two or three matched filters optimized for different-width current signatures.

- Verification tests with SEASAT data indicate that the automated estimation of cross-track geostrophic velocities from residual satellite altimetry is feasible for boundary currents such as the Gulf Stream. The required processing time with the NOSS algorithm is about 1.5 sec per data track with an IBM 4341 computer.

- Both the current-detection and velocity-estimation algorithms yield outputs that are insensitive to isolated data errors.

5.3 SUBJECTS FOR FURTHER STUDY

Based on the results of this investigation, the following subjects are recommended for further study. More detailed suggestions are provided in Sections 2.8, 3.12, and 4.5.

- Develop statistical models for the temporal variations in SEASAT significant-wave-height data and their correlations with the observed mesoscale variability over 3-day intervals in SEASAT repeat-track SSH data.

- For both current detection and velocity estimation, quantify the sensitivity of the NOSS algorithm performance to geoid estimation error.

- Develop a recursive implementation for the matched filter in the NOSS algorithm to provide increased computational efficiency.

- Process all relevant SEASAT altimeter data in the western North Atlantic to provide additional statistics describing NOSS algorithm performance.

APPENDIX A
DERIVATIONS OF MATCHED-FILTER EQUATIONS

This appendix brings together in a consistent notation the derivations of several key results in matched-filter theory. Previously published derivations span a variety of mathematical notations, are scattered in the literature, and do not address the discrete-time theory in detail.

Derivation of Eq. 3.7-20 - The frequency response of the optimal matched filter is (e.g., Ref. 18, pp. 325-329)

$$H(F) = \frac{M(-F)}{S_{NN}(F)} \qquad \text{(A-1)}$$

$M(F)$ = Fourier transform of signature to be detected ($M(-F) = M^*(F)$ = complex conjugate)

$S_{NN}(F)$ = Power spectrum of noise in data.

Let $\chi(t)$ denote the output of the filter at time t. When the data consist of noise only, the mean-square value of $\chi(t)$ is

$$E[\chi^2(t)] = \int_{-\frac{1}{2}}^{\frac{1}{2}} |H(F)|^2 \, S_{NN}(F) \, dF \qquad \text{(A-2)}$$

$$E[\chi^2(t)] = \int_{-\frac{1}{2}}^{\frac{1}{2}} |M(-F)|^2 / S_{NN}(F) \, dF \qquad \text{(A-3)}$$

Since M(-F) = M*(F) = complex conjugate of M(F),

$$E[\chi^2(t)] = \int_{-\frac{1}{2}}^{\frac{1}{2}} \frac{M(-F)}{S_{NN}(F)} M(F)\, dF \qquad (A\text{-}4)$$

$$E[\chi^2(t)] = \int_{-\frac{1}{2}}^{\frac{1}{2}} H(F)\, M(F)\, dF \qquad (A\text{-}5)$$

$$E[\chi^2(t)] = \int_{-\frac{1}{2}}^{\frac{1}{2}} H(F)\, M^*(-F)\, dF \qquad (A\text{-}6)$$

$$E[\chi^2(t)] = \sum_{k=-\infty}^{\infty} h(k)\, m(-k) \qquad (A\text{-}7)$$

where

$$h(k) = \int_{-\frac{1}{2}}^{\frac{1}{2}} H(F)\, e^{i2\pi Fk}\, DF \qquad (A\text{-}8)$$

$$m(k) = \int_{-\frac{1}{2}}^{\frac{1}{2}} M(F)\, e^{i2\pi Fk}\, dF \qquad (A\text{-}9)$$

Therefore, the rms value of the noise in the output of the optimal matched filter is

$$RMS = \sqrt{E[\chi^2(t)]} = \sqrt{\sum_{k=-\infty}^{\infty} h(k)\, m(-k)} \qquad (A\text{-}10)$$

Derivation of Eqs. 3.7-20 and 3.7-21 - The maximum output χ_{max} from the filter specified by Eq. A-1 occurs at time t=0 when the input is m(t)

$$\chi_{max} = \chi(0) = \int_{-\frac{1}{2}}^{\frac{1}{2}} X(F)\, dF \qquad \text{(A-11)}$$

where

$$X(F) = \sum_{t=-\infty}^{\infty} \chi(t)\, e^{-i2\pi Ft} \qquad \text{(A-12)}$$

But $X(F) = H(F)\, M(F)$, therefore

$$\chi_{max} = \int_{-\frac{1}{2}}^{\frac{1}{2}} H(F)\, M(F)\, dF \qquad \text{(A-13)}$$

Comparing Eq. A-13 with Eq. A-5 shows that

$$\chi_{max} = E[\chi^2(t)] \qquad \text{(A-14)}$$

This result can be rewritten as follows by using Eq. A-10

$$\chi_{max} = RMS^2 \qquad \text{(A-15)}$$

The rms signal-to-noise ratio (SNR) is defined as

$$SNR = \frac{\chi_{max}}{\sqrt{E[\chi^2(t)]}} \qquad \text{(A-16)}$$

Substituting Eqs. A-15 and A-10 in Eq. A-16 yields

$$SNR = \frac{RMS^2}{RMS} = RMS \qquad \text{(A-17)}$$

which verifies Eq. 3.7-20. Equation 3.7-21 is verified by using Eq. A-17 to rewrite Eq. A-15 as

$$\chi_{max} = SNR^2 \tag{A-18}$$

Derivation of Eq. 3.7-23 - Let U(t) denote the unit step function defined as

$$\begin{aligned} U(t) &= 1 \text{ for } t \geq 0 \\ U(t) &= 0 \text{ for } t < 0 \end{aligned} \tag{A-19}$$

The average number C(N) of zero crossings in N samples of a stationary time series $\{X_k\}$ is

$$C(N) = \frac{1}{N} \sum_{k=1}^{N} U(-X_k\ X_{k+1}) \tag{A-20}$$

The mean frequency F_m of $\{X_k\}$ is defined as half the expected value of C(N)

$$F_m = \frac{1}{2} E[C(N)] = \frac{1}{2N} \sum_{k=1}^{N} E[U(-X_k\ X_{k+1})] \tag{A-21}$$

Because $\{X_k\}$ is stationary, the expectation in Eq. A-21 is independent of k. Therefore, Eq. A-21 may be written as

$$F_m = \frac{1}{2} E[U(-X_k\ X_{k+1})] \tag{A-22}$$

But $E[U(-X_k\ X_{k+1})]$ = Probability that $X_k\ X_{k+1} < 0$, which is expressed as

$$F_m = \frac{1}{2} \text{ Prob } \{X_k\ X_{k+1} < 0\} \tag{A-23}$$

Let

$$r = R_{xx}(1)/R_{xx}(0) \tag{A-24}$$

where $R_{xx}(k)$ is the autocorrelation sequence of X_k:

$$R_{xx}(k) = E\,[X_{j+k}\,X_j] \tag{A-25}$$

The analysis in Ref. 17, p. 199, shows that

$$\text{Prob}(X_k\,X_{k+1} < 0) = B/\pi \tag{A-26}$$

$$B = \cos^{-1}(r) \tag{A-27}$$

From Eqs. A-23, A-26, and A-27, it follows that

$$F_m = \frac{\cos^{-1}(r)}{2\pi} \tag{A-28}$$

The last step in this derivation is to establish a formula for parameter r, which is valid when $\{X_k\}$ is the output of an optimal matched filter with frequency response H(F) (Eq. A-1) that is driven by zero-mean Gaussian noise with power spectrum $S_{NN}(F)$. The power spectrum $S_{xx}(F)$ of $\{X_k\}$ is

$$S_{xx}(F) = |H(F)|^2\,S_{NN}(F) \tag{A-29}$$

In view of Eq. A-1, Eq. A-29 may be written as

$$S_{xx}(F) = \frac{|M(-F)|^2}{S_{NN}(F)} \tag{A-30}$$

But $|M(-F)|^2 = M(-F)\,M(F)$ because m(k) is real. Therefore

$$S_{xx}(F) = \frac{M(-F)}{S_{NN}(F)}\,M(F) \tag{A-31}$$

$$S_{xx}(F) = H(F)\,M(F) \tag{A-32}$$

Taking the inverse Fourier transform of Eq. A-32 yields the following expression for the autocorrelation sequence of the output noise

$$R_{xx}(k) = \sum_{j=-\infty}^{\infty} h(j)\, m(k-j) \qquad \text{(A-33)}$$

$h(k)$ = Impulse response of filter

$m(k)$ = Signature to be detected

With this result, it follows from Eqs. A-10 and A-17 that

$$R_{xx}(0) = SNR^2 \qquad \text{(A-34)}$$

Let $x = R_{xx}(1)$, then

$$x = \sum_{j=-\infty}^{\infty} h(j)\, m(1-j) \qquad \text{(A-35)}$$

Combining Eqs. A-34, A-35, A-24, and A-28 yields the desired result:

$$F_m = \frac{1}{2\pi} \cos^{-1}(x/SNR^2) \qquad \text{(A-36)}$$

REFERENCES

1. Huang, E.N., and Leitao, C.D., "Large-Scale Gulf Stream Frontal Study Using GEOS-3 Radar Altimeter Data," J. Geophys. Res., Vol. 83, No. C9, 20 September 1978, pp. 4673-4682.

2. Marsh, G.J., Martin, T.V., McCarthy, J.J., and Chovits, P.S., "Estimation of Mean Sea Surfaces in the North Atlantic, the Pacific and the Indian Ocean Using GEOS-3 Altimeter Data," NASA Tech. Memo. 79704, Goddard Space Flight Center, February 1979.

3. Leitao, C.D., Huang, N.E., Parsons, C.L., Parra, C.G., McMillan, J.D., and Hayne, G.S., "Final Report of GEOS-3 Radar Altimeter Study for the South Atlantic Bight," NASA Tech. Memo. 73286, Wallops Flight Center, May 1980.

4. Cheney, R.E., Marsh, J.G., and Grano, V., "Global Mesoscale Variability from SEASAT Collinear Altimeter Data," EOS, Amer. Geoph. Union., Vol. 62, No. 17, 1981, p. 298.

5. Leitao, C.D., and Huang, N.E., "A Note on the Comparison of Radar Altimetry with IR and In Situ Data for the Detection of the Gulf Stream Surface Boundaries," J. Geophys. Res., Vol. 84, No. B8, 30 July 1979, pp. 3969-3973.

6. Cheney, R.E., and Marsh, J.G., "SEASAT Altimetry Observations of Dynamic Ocean Currents in the Gulf Stream Region," J. Geophys. Res., Vol. 86, No. 1, January 1981, pp. 473-483.

7. Richardson, P.L., Cheney, R.E., and Worthington, L.V., "A Census of Gulf Stream Rings, Spring 1975," J. Geophys. Res., Vol. 83, No. C12, December 1978, pp. 6136-6143.

8. Marsh, J.G., and Cheney, R.E., personal communication.

9. Gray, A.H., and Markel, J.D., "Linear Prediction Analysis Programs (AUTO-COVAR)," Programs for Digital Signal Processing, edited by the Digital Signal Processing Committee, IEEE Acoustics, Speech, and Signal Processing Society, John Wiley & Sons, New York, 1979, pp. 4.1-1 - 4.1-7.

REFERENCES (Continued)

10. Akaike, H., "A New Look at the Statistical Model Identification," IEEE Trans. Automat. Contr., Vol. AC-19, No. 6, December 1974, pp. 716-723.

11. Akaike, H., "Canonical Correlation Analysis of Time Series and the Use of an Information Criterion," System Identification: Advances and Case Studies, R.K. Mehra and D.G. Lainiotis (Editors), Academic Press, New York, 1976, pp. 27-96.

12. Akaike, H., "A Bayesian Extension of the Minimum AIC Procedure of Autoregressive Model Fitting," Biometrica, Vol. 66, No. 2, 1979, pp. 237-242.

13. Gelb, A. (editor), Applied Optimal Estimation, The MIT Press, Cambridge, 1974.

14. Marsh, J.G., and Chang, E.S., "5' Detailed Gravimetric Geoid in the Northwestern Atlantic Ocean," Marine Geodesy, Vol. 1, No. 3, 1978, pp. 253-261.

15. Helstrom, C.W., Statistical Theory of Signal Detection, Second Edition, Pergamon Press, Oxford, 1968.

16. Whalen, A.D., Detection of Signals in Noise, Academic Press, New York, 1971.

17. Papoulis, A., Probability, Random Variables, and Stochastic Processes, McGraw-Hill, New York, 1965.

18. Papoulis, A., Signal Analysis, McGraw-Hill, New York, 1977.

19. White, J.V., "NOSS Algorithm Specifications for Ocean Current Mapping," The Analytic Sciences Corporation, Report No. TR-3764-1, January 1982.

20. Douglas, B.C., and Cheney, R.E., "Ocean Mesoscale Variability from Repeat Tracks of GEOS-3 Altimeter Data," J. Geophys. Res., Vol. 86, No. C11, November 1981, pp. 10931-10937.